This article has been accepted for inclusion in a future issue of this journal. Content is final as presented, with the exception of pagination.



# An Approach to the Assessment of Detectability of Subsurface Targets in Polar Ice From Satellite Radar Sounders

Sanchari Thakur, *Member, IEEE*, Elena Donini, *Member, IEEE*, Francesca Bovolo, *Senior Member, IEEE*, and Lorenzo Bruzzone, *Fellow, IEEE*

***Abstract*— A satellite mission onboard a radar sounder for the observation of the earth's polar regions can greatly support the monitoring of the cryosphere and climate change analyses. Several studies are in progress proposing the design and demonstrating the performance of such an earth-orbiting radar sounder (EORS). However, one critical aspect of the cryospheric targets that are often ignored and simplified in these studies is the complex geoelectrical nature of the polar ice. In this article, we present a performance assessment of the polar ice target detectability by focusing on their realistic representation. This is obtained by simulating the orbital radargrams corresponding to different regions of the polar cryosphere by leveraging the data available from airborne campaigns in Antarctica and Greenland. We propose novel performance metrics to analyze the detectability of the internal reflecting horizons (IRHs), the basal interface, and to analyze the nature of the basal interface. This performance assessment strategy can be applied to guide the design of the signal-to-noise ratio (SNR) budget at the surface, which can further support the selection of the main orbital instrument parameters, such as the transmitted power, the two-way antenna gain, and the processing gains.**

***Index Terms*— Cryosphere, earth observation, radar design, radar sounder, remote sensing, simulation, target detection.**

## NOMENCLATURE

| | |
|---|---|
| $P_{r,A}(r_A, c_A)$ $P^b_{r,E}(r_E, c_E)$ | ARS/simulated EORS received power (in dB) radargrams. |
| $r_A$ $r_E$ | ARS/EORS sample index. |
| $c_A$ $c_E$ | ARS/EORS frame index. |
| $\gamma_{\mathrm{SS},A}(z)$ $\gamma_{\mathrm{SS},E}(z)$ | ARS/EORS subsurface target propagation factor in dB. |
| $\gamma_{S,A}$ $\gamma_{S,E}$ | ARS/EORS surface reflectivity in dB. |
| $H_A$ $H_E$ | ARS/EORS platform altitude. |
| $G_A^2$ $G_E^2$ | ARS/EORS two-way antenna gain in dB. |
| $\lambda_A$ $\lambda_E$ | ARS/EORS wavelength in meters. |
| $P_{t,A}$ $P_{t,E}$ | ARS/EORS transmitted signal power in dB. |
| $G_{r,A}$ $G_{r,A}$ | ARS/EORS range processing gain in dB. |
| $G_{\mathrm{az},A}$ $G_{\mathrm{az},E}$ | ARS/EORS azimuth processing gain in dB. |
| $f_{c,A}$ $f_{c,E}$ | ARS/EORS central frequency in Hz. |
| $n_+$ $n_-$ | labels assigned by the classifier to the basal interface samples corresponding to lakes (+) and nonlakes (−). |
| $c$ $\gamma$ | kernel parameters of the subglacial lakes support vector machine (SVM) classifier. |
| $\ell_{\mathrm{ARS}}$ $\ell_{\mathrm{EORS}}$ | predicted labels of the basal interface obtained by applying the SVM classifier to the ARS and EORS data, respectively. |
| $\xi_{\mathrm{ARS}}$ $\xi_{\mathrm{EORS}}$ | vectors representing correct prediction of the nature of the basal interface in the ARS and EORS data. |
| $k$ | Boltzmann's constant. |
| $T_{\mathrm{cmb}}$ | galactic noise temperature in K, (subscript CMB implies cosmic microwave background). |
| $\rho(z, c_A)$ | target subsurface reflectivity profile in dB for the frame $c_A$ as a function of depth $z$. |
| $\alpha(z)$ | target attenuation profile independent of the frequency. |
| $\eta$ | Cole–Cole distribution parameter (frequency-dependence factor). |
| $z$ | depth below surface. |
| $L$ | label corresponding to the geographical zone (geolabel). |
| $N_E^L$ | total number of frames corresponding to the label $L$. |
| $c_E^L$ | frame index corresponding to the label $L$. |
| $b$ | simulation index corresponding to each hypotheses of the variable design parameter. |

Manuscript received October 28, 2020; revised February 24, 2021, April 8, 2021, June 5, 2021, and July 11, 2021; accepted October 6, 2021. This work was supported by the Italian Space Agency (ASI) through the project "Attività scientifiche per JUICE fase C/D" under Grant ASI 2018-25-HH.0. *(Corresponding author: Lorenzo Bruzzone.)*

Sanchari Thakur and Lorenzo Bruzzone are with the Department of Information Engineering and Computer Science, University of Trento, 38123 Trento, Italy (e-mail: lorenzo.bruzzone@unitn.it).

Elena Donini and Francesca Bovolo are with Fondazione Bruno Kessler, 38123 Trento, Italy.

Digital Object Identifier 10.1109/TGRS.2021.3119047

| | |
|---|---|
| $N_b$ | total number of hypotheses of the variable design parameter. |
| $\mathrm{SNR}_b$ | hypotheses values of the variable design parameter–SNR budget in dB. |
| $\theta_b(c_E)$ | IRH detection performance metric estimated as the probability of IRH detection for the EORS frame $c_E$ corresponding to the simulation index $b$. |
| $\theta$ | IRH detection probability threshold. |
| $\chi_b^L(\theta)$ | cumulative fraction of frames with probability of IRH detection greater than $\theta$ for the geolabel $L$ and simulation index $b$. |
| $\beta_b(c_E)$ | basal interface detection metric for each frame $c_E$ and simulation index $b$. |
| $\Lambda_b(c_E)$ | lake detection metric comparing the accuracy of the subglacial lake detection for the EORS and ARS radargrams. |
| $\beta_b^L$ | cumulative basal interface detection metric, i.e., fraction of frames for which the basal interface detection metric is equal to 1 for the geolabel $L$ and simulation index $b$. |
| $\theta_{\min}^L$ | minimum required per-frame probability of IRH detection for the geolabel $L$. |
| $\chi_{\min}^L$ | requirement on the cumulative fraction of frames satisfying the per-frame probability of IRH detection for the geolabel $L$. |
| $\beta_{\min}^L$ | requirement on the basal interface detectability for the geolabel $L$. |
| $\mathrm{SNR}_{\min}$ | minimum required SNR budget for a given set of mission requirements and estimated for each geolabel. |
| $\mathrm{SNR}_{\mathrm{design}}$ | best design parameter that maximizes the performance for all geolabels for a given set of mission requirements. |

## I. Introduction

The earth's polar ice sheets are crucial components of the cryosphere that affects global climate change and sea-level rise. Several cryohydrodynamic processes occurring at the base of the ice sheets affect the stability and seaward flow of the ice. Direct measurement and imaging of the ice sheet down to the base are essential for studying these processes and modeling the stability of the ice sheets. This can be appropriately achieved by profiling the ice using radar sounders (RSs), also referred to as ice-penetrating radar. Considering the need for RS data for imaging the polar ice caps, several airborne RS (ARS) campaigns have been conducted in Antarctica and Greenland [1], [2]. Relevant scientific returns have been obtained from data acquired by these campaigns, such as: 1) estimation of the thickness of the ice sheets; 2) analysis of the internal reflecting horizons (IRHs); 3) detection of subglacial lakes [3]; 4) analysis of basal flow regime [4]; and 5) identification of basal refreezing [5]. However, these acquisition campaigns are expensive and time-consuming, and despite a large number of campaigns, radar profiles are absent over very large portions of the polar areas (e.g., 500 000 km$^2$ of Antarctica), resulting in incomplete information on the polar ice characteristics [6]. Moreover, since the data are collected in one-time campaigns with local coverage to study specific phenomena, repeat-pass acquisitions are also not available. Furthermore, due to the use of different instruments and airborne platforms, the data quality strongly varies between the different campaigns.

An earth-orbiting radar sounder (EORS) operating from a satellite platform can address the limitations posed by the airborne campaigns by providing homogeneous data quality with uniform and multitemporal coverage of the earth. However, at orbiting altitudes, RSs are subjected to many performance-limiting factors. These mainly include: 1) the propagation losses due to the large distance to the target; 2) the distortions caused by the ionosphere; 3) the surface clutter due to a relatively large antenna footprint; 4) the presence of galactic noise; and 5) frequency band allocation required for earth observation. Many of these factors can be mitigated at the system design level or in postprocessing to ensure the extraction of valuable scientific information, as successfully demonstrated by the current heritage of planetary RSs (SHARAD [7] and MARSIS [8] on Mars, LRS [9] on the Moon, RIME [10], and REASON [11] scheduled for the Jovian icy moons).

Leveraging the heritage of terrestrial airborne and planetary RSs, currently, studies are in progress for the proposal of an orbital RS, operating in the HF–VHF bands [12]–[15]. These studies are based on assessing the performance of a given orbital design in detecting the critical targets and achieving the scientific goals of the mission. These assessments are used to guide the selection of the instrument parameters by determining the appropriate tradeoff between the achievable performance and the technical and physical limitations [16]. Many of these studies focus on understanding the impact of the earth's ionosphere [13], [14], [17], the surface clutter [6], [15], and the capability to penetrate up to the base of the ice sheet (assuming homogeneous dielectric properties of the ice) [12].

However, only a few of these studies (e.g., [6], [15]) assess the performance considering the structural details of the targets (such as the IRHs), which are both: 1) a performance-limiting factor (e.g., in terms of subsurface scattering and attenuation losses) and 2) a detection objective of the instrument. Given the need to analyze the detectability of the cryospheric targets, it is imperative to model and simulate their radar response. The complex dielectric permittivity profile of the ice depends on several factors, such as the presence of impurities (e.g., dust, ash, rocks, salts, and acids), the crystal orientation fabric, the thermal profile, and the distribution of melt-zones. The high variability of these factors over unknown spatial scales and the lack of geophysical models to translate them to the corresponding electrical properties make it difficult to subjectively define the dielectric profile of the ice. This inhibits their assessment using conventional 3-D electromagnetic RS simulators [18]–[20]. Recently, a novel simulation approach has been proposed, which is based on reprocessing the radargrams acquired over geological analogs of the target [21].

In this article, we adopt this simulation approach based on reprocessing the airborne data to predict orbital performance. The airborne data are a rich source of information of the targets due to: 1) the availability of large archives of data from multiple campaigns [1], [2]; 2) the widespread and full-depth coverage of the Antarctic and Arctic ice sheets; and 3) the similarity with the actual radar signatures of complex cryospheric targets (principles of operation of the airborne and the orbital RS are similar). The input airborne data are selected to represent different regimes on Antarctica and Greenland, i.e., grounded ice, floating ice, and subglacial lakes. The performance assessment analyzes the achievability of the main objectives of an orbital RS mission: 1) detectability of IRHs; 2) detectability of the basal interface; and 3) characterization of the nature of the basal interface.

Assuming the feasible range of central frequency and bandwidth provided by the previous studies, the proposed detailed assessment of detectability of the targets is aimed at revealing the required signal-to-noise ratio (SNR) budget at the surface that maximizes the detectability of these three target categories. The required SNR budget can guide the selection of main instrument parameters, such as the two-way antenna gain and the transmitted power. These parameters can support the optimization of the orbital sensor configuration, such as in the case of a recently proposed distributed orbital RS architecture [22].

This article is structured as follows. Section II illustrates the previous studies on the challenges of the orbital RS design, i.e., ionospheric distortion, surface and firn scattering, volume scattering losses, galactic noise, and the structure of the target. Section III describes the proposed approach to the design and performance analysis of orbital RSs, focusing on: 1) the limitation of state-of-the-art studies; 2) the orbital RS simulation approach; 3) the extraction of the ice targets from the simulated orbital radargrams; and 4) the evaluation of target detection performances. Section IV focuses on the description of the datasets used in the study and the experimental results. Finally, Section V concludes this article and discusses future works.

## II. Challenges of Orbital Sounding of the Earth

Airborne RSs have successfully demonstrated that subsurface targets of scientific interest in the ice (IRHs, basal interface, basal flow regimes, and so on) can be detected and interpreted (e.g., [5], [23]–[25]). However, extending this capability of sounding the earth's cryosphere to orbital platforms requires addressing some challenges related to the detectability of the targets. The earth's ionosphere has a peak electron density at an altitude of 200–400 km that can distort the received signal during propagation. Orbital altitudes are typically larger than 500 km, which implies that the signal transmitted from satellite platforms has to propagate through the earth's ionosphere twice before the reception. At orbital altitudes at relatively low frequencies, the antenna footprint is larger, and incidence angles are smaller, resulting in a critical signal-to-clutter ratio (SCR). The large distance between the RS and the target results in higher propagation losses. Beyond the earth's atmosphere, radar sounding is impacted by the high levels of galactic noise, which is absent in airborne sounding. These factors contribute also to degrade the range resolution and the subsurface SNR and must be considered while designing the orbital RS. Another component that further complicates the design of the orbital RS is the highly complex nature of the target.

The design of the existing and scheduled RSs for planetary bodies is based on a tradeoff analysis between the achievable performance given a set of design constraints (instrument and orbit characteristics) and the limitations imposed by the physical scenario (target and environment) [7], [8], [10], [16].

For an orbital RS, previous feasibility studies considered two end-member design concepts: 1) an RS system in VHF band operating at the central frequency of 45 MHz [12]–[14], [17] and 2) an RS system in P-band operating at a central frequency of 435 MHz [6], [15]. The choice of these two bands is justified by the tradeoff between penetration and range resolution, constrained by the ionospheric cutoff frequency and clutter mitigation. A proper frequency choice can significantly improve clutter mitigation [6], [15], [26]–[28]; about 40 dB improvement in firn clutter suppression can be obtained with the 45-MHz sounder compared to a P-band one [6]. As for the 45-MHz system, clutter only limits the detection of IRHs deeper than 3000 m [6]. On the one hand, the VHF band can reasonably mitigate the effects of propagation through the earth's ionosphere while providing high penetration capability. On the other hand, the P-band is the lowest possible frequency currently allocated by the International Telecommunication Union (ITU) for earth observation. With this view, the allocation of the VHF band for earth observation is included in the preliminary agenda of the 2023 World Radio-Communication Conference. In this context, this section will analyze and discuss some of the critical design challenges for an orbital RS, reviewing the previous studies and design concepts.

### A. Propagation Through the Ionosphere

The ionosphere interacts with the signal by introducing distortions in the radargrams that critically affect the phase and the range resolution. These effects are more pronounced at low frequencies, and sounding is impossible at frequencies lower than the plasma frequency of the ionosphere. For the earth's ionosphere, Freeman *et al.* [14] showed that the cutoff frequency is less than 4 MHz at all latitudes at the solar minimum at 4 AM local time. Even while operating at frequencies much higher than the cutoff (e.g., 40–50 MHz), the received signal can still be distorted in terms of loss of signal power, Faraday rotation of linearly polarized waves, propagation delays leading to uncertainties in the range and phase of the signal, phase dispersion, loss of coherence time, and phase and amplitude variations caused by scintillation (changes in the electron density). Nevertheless, Freeman *et al.* [14] show that, for a signal with a central frequency of 45 MHz and bandwidth of 10 MHz, most of these effects can be tolerable and mitigated with an appropriate design and with data correction.

For example, the Faraday rotation effects can be mitigated by using a circularly polarized signal instead of linear polarization, and the irregularities in the ionosphere occur less than 10% of the time. Moreover, statistical analyses of observations in polar regions show that scintillations causing high power fading have a very low probability of occurrence around the solar minimum; their RMS phase error is lower than 30° more than 50% of the times (depending on the solar zenith angle), which implies a loss of less than 0.2 dB in the gain obtained by coherent integration.

These qualitative assessments of the ionospheric effects were quantitatively analyzed considering the 45-MHz central frequency RS [17]. The authors demonstrated the feasibility of mitigating these effects with a compensation technique based on Legendre polynomials. The study considered the range of expected ionospheric parameters, namely, the total electron count (TEC) and the magnetic field intensity. The impact of the ionosphere on the: 1) peak-to-sidelobe ratio; 2) loss of peak power; and 3) loss of range resolution by the main lobe widening is estimated. The compensation approach was based on estimating the TEC values. The authors concluded that the distortion effects can be effectively compensated depending on the accuracy of the parameter estimation; at less than 5% error on the TEC values, the resolution loss factor is nearly 0, and the power loss is less than 1 dB during most of the solar cycle.

The analysis of the ionospheric effects and the satisfactory performance obtained at the 45-MHz central frequency with a bandwidth of 10 MHz, especially when operating close to the solar minimum, are the basis of the orbiting arid subsurface and ice sheet sounder (OASIS) [13] and the SaTellite Radar sounder for earth sUbsurface Sensing (STRATUS) [12] mission concepts.

### B. Surface and Firn Scattering

The reflections from off-nadir surface structures can potentially mask the nadir subsurface target reflections in radargrams. The impact of surface clutter and its increase with the increase in platform elevation and the radar frequency was studied by airborne sounding over an ice stream in Greenland at two altitudes (500 and 4400 m) and operating at two central frequencies (150 and 450 MHz) [28]. The study found that surface clutter is the primary scattering mechanism that can obscure the basal interface and limits the choice of higher frequencies. To evaluate the impact of clutter at orbital altitudes and, therefore, the feasibility of a P-band orbital sounder for the earth, Dall *et al.* [15] and [29] acquired data using the POLarimetric Airborne Radar Ice Sounder (POLARIS) campaign in Antarctica. Electromagnetic models of the ice targets were extracted from the POLARIS radargrams and integrated with ancillary information on the attenuation properties. These models were used to evaluate the SNR and SCR of the IRHs and the basal interface, using the radar equation. The authors concluded that surface and within-ice volume clutter (from the firn layer) are the primary factors limiting the detectability of the basal interface (in two-third of the considered scenarios in Antarctica, the bed was not detectable).

In a recent study, the contribution of firn clutter has been analyzed in detail by first determining the most appropriate physical model defining the firn layer, followed by simulating and comparing the SCR and SNR achievable at central frequencies of 45 and 435 MHz, with variable bandwidths [6]. The performance simulations at different frequencies show that very high fractional bandwidths are needed at UHF frequencies to maintain the firn clutter at a 25-dB level below the surface power. They recommend orbital sounding at frequencies below 80 MHz to suppress the impact of near-surface firn clutter. Moreover, it is found that the SCR of the 45-MHz radar is significantly better, the basal interface detection is not affected by clutter, and only the IRHs deeper than 3000 m may have critically low SCR to be detected [6].

Nevertheless, several techniques can mitigate the issues with clutter at design and processing levels. Fully focused SAR processing reduces along-track clutter. Novel RS architectures, such as the distributed RS, can drastically reduce cross-track clutter [22]. There are also several clutter discrimination approaches based on coregistering the radargrams with the simulated cluttergrams [30]–[32], using single-pass interferometry [33] or exploiting the polarization signatures [34]. Another interesting approach draws inspiration from the clutter discrimination capabilities of big brown bats [35] and exploits the split spectrum and frequency differences for distinguishing between surface and subsurface reflections.

### C. Volume Scattering Losses

Volume scattering was considered to be the main contributor to firn clutter in POLARIS data and, therefore, a critical performance-limiting factor in orbital sounding at UHF frequencies [29]. This interpretation was based on the assumption that firn can be modeled as composed of distributed pores that result in incoherent backscattering of the signal power. Culberg and Schroeder [6] analyzed the validity of this assumption by comparing the electromagnetic models of dry firn obtained from ice-core data with airborne radar profiles acquired by MCoRDS (central frequency of 195 MHz) [1] and Accumulation Radar (central frequency of 725 MHz) [36]. They concluded that the firn is best modeled as composed of quasi-specular layers with small-scale roughness (thus contributing to firn clutter, as described in Section II-B) rather than a contributor to volume scattering.

The study presented in [6] further evaluated the backscattered power in the 40–50-MHz band by assuming air-filled spherical pores with radii ranging from 1 mm to 1 cm, with realistic porosity derived from ice cores, and found the volume scattering contribution to be at least 40 dB below the surface power. The authors also studied the two-way attenuation losses due to volume scattering assuming density inhomogeneities and found the losses to be even lower (less than a few dB at HF frequencies). Therefore, these experiments concluded that, for the VHF radar, volume scattering is not a major impeding factor in the detection performance.

### D. Ability to Resolve the Target Signal From Noise

The galactic noise temperatures at the VHF band and the P-band are 6320 and 19.6 K, respectively [37].

The corresponding noise power levels are −120 and −135 dBW, respectively, which indicates that, at the VHF frequencies, the galactic noise levels are 15 dB higher than at the P-band. Thus, previous studies [6], [12], [15] have identified that, for an orbital ice-sounding radar operating at a central frequency of 45 MHz, SNR is a more critical factor than SCR in the detectability of the targets. Accordingly, the galactic noise levels have been considered while projecting the penetration performance of OASIS [13] and STRATUS [12]. At the design level, mitigating these noise levels needs increasing the transmitted power and antenna gain, and improving the effectiveness of along-track processing by increasing the integration length and by choosing appropriate PRF and pulsewidth.

Many of these technical requirements can be fulfilled by using a distributed architecture based on a flying formation, as elucidated in [22]. With regards to the effectiveness of the along-track processing, the impact of RS acquisitions from orbital altitudes on the SNR was studied in [38]. The authors modeled a point target located 2 km below the ice surface and simulated its radar response to a P-band RS flying at two different altitudes: 1) an airborne altitude of 1 km and 2) an orbital altitude of 500 km. The study showed that in the case of orbital sounding, the SNR improvement due to SAR focusing is not as significant as with the airborne one. Nonetheless, the improvement in the along-track resolution is achievable with an orbital RS.

### E. Complex Structure of the Target

The polar ice strata have very complex structural and compositional properties, as revealed by several ice-core data, observations of outcrops, GPR, and airborne campaigns (e.g., [5], [23]). The ice subsurface is characterized by a finely layered structure representing paleoclimatic records of seasonal accumulation and deposition of snow, interbedded by various impurities. The thickness, topography, and composition of these IRHs are highly variable, thus inhibiting the precise and uniform modeling of the ice targets across the entire polar ice.

The target geoelectrical models (representing structure, composition, and dielectric properties) play a crucial role in predicting radar detection performance. Previous studies proposing the orbital mission concept were based on evaluating the radar equation, assuming a specular ice surface and basal interface, and a homogeneous dielectric medium [12], [13]. Dall *et al.* [15] show that this assumption is not valid for terrestrial ice, which is certainly highly heterogeneous in the top few hundred meters.

Ice-core dielectric and density profiles, as well as airborne radar profiles, have been used in some studies to derive realistic physical models of the targets [6], [15], [39] for understanding their detectability. Other studies went a step further and used the ice-core data to generate models for 3-D electromagnetic simulations of the radar response of GPR instruments [40], [41]. While these studies pave the way to the accurate modeling and simulation of RS response of the ice targets, the sparse sampling and shallow depth of ice-cores limits their use in continent-wide estimation of detection performance. To the best of our knowledge, there is no study on the detection performance of IRHs with an orbital RS over large areas of the polar ice caps, especially at 40–50-MHz frequencies.

Based on the studies summarized in this section, an orbital RS operating at a central frequency of 45 MHz with a bandwidth of 10 MHz will be able to minimize the distortions caused by the ionosphere and surface clutter while maintaining the range resolution required for discriminating the IRHs. The studies also indicate that the SNR degradation caused by galactic noise levels may be a limiting factor for the 40–50-MHz orbital RS and may affect the detectability of the IRHs and the basal interface, which has not been studied so far.

## III. Methodology

### A. Limitations of the Previous Studies

Although several performance-limiting factors, such as the ionosphere and firn clutter, have been deeply analyzed in the previous works, there is a lack of studies considering the targets in detail. Regarding the targets, the existing literature on orbital RS design has several limitations:

1) Polar ice is strongly nonhomogeneous and has high spatial variability in the structure up to the centimeter scale. The resulting variability in the subsurface scattering losses and dielectric attenuation profiles [42], [43] translates to significant spatial variability in the radar penetration capability. Thus, it is necessary to study the impact of this variability on the retrieval of the ice-thickness across different regions.
2) Detectability of the IRHs is critical for the science goals of an orbital mission to model historical records of processes occurring within the ice. While ice-core data provides detailed information on the IRHs with a resolution of a few centimeters, achieving such levels of detail from an orbiting platform is technically insurmountable. However, the goal of orbital RS profiling is to image the prominent IRHs detectable at the feasible bandwidth with sufficient SNR. The existing orbital studies usually assume a homogeneous target and ignore the IRHs;
3) To support the scientific goals of an orbital mission, it is not only required to detect the basal interface (i.e., to penetrate the full thickness of the ice) but also to characterize its geophysical properties. This includes detecting geological targets within the ice column and extracting information on the glacier processes, such as the mapping of the water distribution at the basal interface (e.g., basal flow regime and subglacial lakes). This is of critical importance for predicting the stability of the ice sheets and the rate of seaward flow of the ice. Such analyses require detailed geoelectrical modeling of the targets, rather than considering a homogeneous structure.

This article aims to address these limitations by proposing an approach to the assessment of the detection performance of an orbital RS considering a realistic representation of the polar ice targets. The target modeling is handled in a nonsubjective and automatic way by leveraging the airborne data and using them as inputs to an airborne-to-satellite radargram

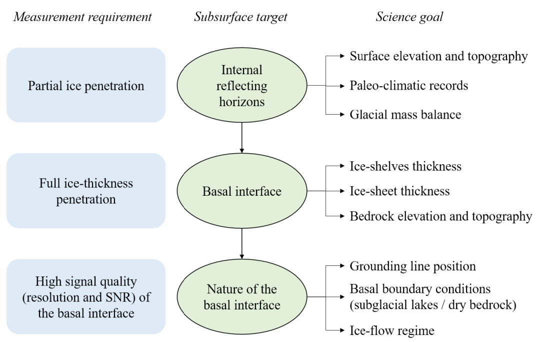


Fig. 1. Hierarchical performance analysis of the targets based on progressively increasing measurement requirements and achievability of the science goals of subsurface sounding of the polar ice.

simulation technique. This allows us to account for the IRHs and the spatial variability in the dielectric properties. The simulation of the orbital radargrams also enables an assessment of the automatic interpretability of the detected targets and, thus, demonstrates the scientific feasibility of the mission.

## *B. Science Goals of Orbital Sounding: A Hierarchical Approach to the Performance Analysis*

From the perspective of the scientific objectives of subsurface sounding of the polar ice and the nature of the related targets, a hierarchical relationship between the radar performance and the target detectability can be observed (see Fig. 1). At a preliminary level of performance, an important scientific requirement of polar ice sounding is that the prominent near-surface IRHs should be mapped. This requires penetration through the top part of the ice and with sufficient power so that signal received from the IRHs is above the noise and the off-nadir clutter levels. The detectability of the IRHs is significant for inferring the paleoclimatic models and the ice mass balance.

In the next higher level of performance, the orbital RS should be able to delineate the basal interface, representing the interface between ice–bedrock (for grounded ice) or ice–water (subglacial lakes, i.e., grounded ice having a large pool of melt-water at the base, or floating ice). This requires a penetration capability higher than the full ice thickness, overcoming the scattering and power attenuation losses caused by the ice. The detected basal interface can be used to estimate the thickness of ice sheets and ice shelves, and generate the 3-D topography of the bedrock (which can also support other relevant scientific studies, such as detection of buried craters [44], [45]).

Finally, for extracting scientifically valuable information from the data acquired by the mission, it is not only necessary to detect the prominent dielectric interfaces but also to accurately interpret the geophysical properties characterized by these interfaces (e.g., composition, structure, and dielectric properties). Such studies have been widely applied to the airborne radargrams, such as to the automatic detection of subglacial lakes [24] and mapping of basal units [25]. In this context, if the requirement on the penetration through the full ice thickness is satisfied, a higher level of performance

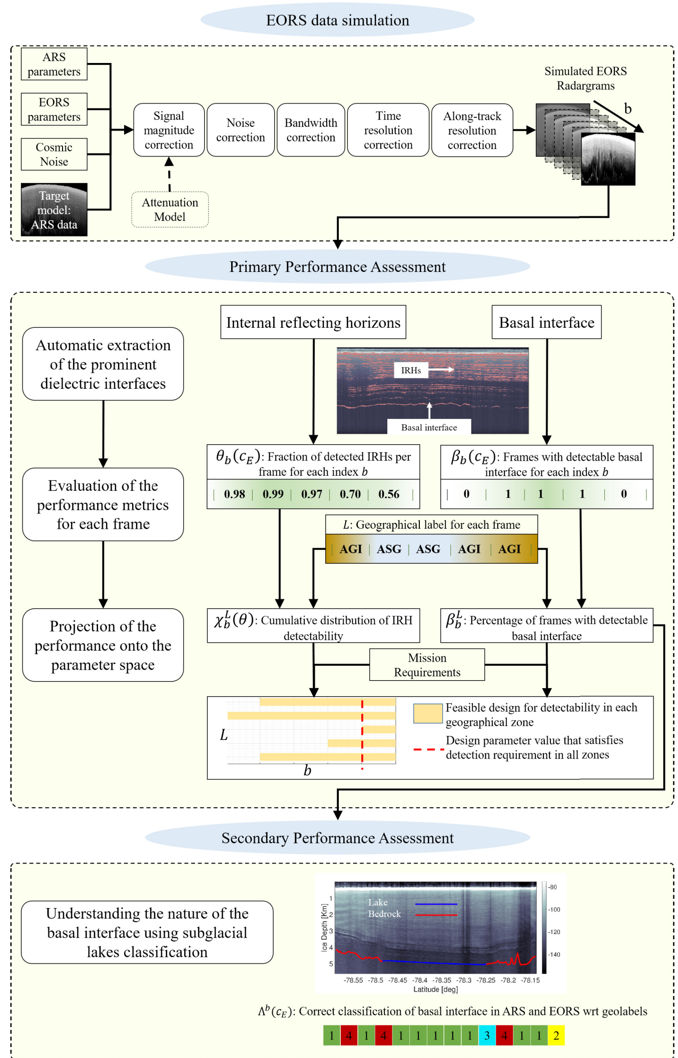


Fig. 2. Flowchart of the proposed methodology.

requires the interpretation of the basal conditions (e.g., presence or absence of subglacial lakes, subglacial channel-flow, and accreted ice). This is possible only if the SNR of the signal received from the base is sufficiently high, and there are adequate range and along-track resolutions. Identifying the nature of the basal interface (such as ice–freshwater, ice–sea water, and ice–bedrock) can support the inference of the grounding line position, basal boundary conditions, and the ice-flow regime.

## *C. Proposed Approach*

Fig. 2 shows the schematic of the proposed methodology. The notation and symbols used to describe the method are listed in Nomenclature. In particular, the subscripts $A$ and $E$ are used to represent the airborne and orbital cases, respectively. The first step involves the preparation of the simulation inputs, that is: 1) a database of airborne radargrams (downloaded and preprocessed); 2) the corresponding airborne instrument parameters; 3) definition of the design orbital parameters; and 4) the corresponding levels of cosmic noise power.

Since the structural and geophysical properties of the ice targets vary with their location, we have selected the input ARS radargrams widely distributed in different geographical conditions. To separately analyze the radar performance in each of the geographical settings, we have defined five principal geographical zones based on the known differences in the dielectric and radar characteristics of the basal interfaces [24], [43], [46] and properties of the IRHs. These zones include grounded ice (interior of the ice sheets having an ice–bedrock interface), floating ice (coastal ice shelves and floating ice-tongues having ice–seawater interface), and subglacial lakes (ice–freshwater interface). These are further segregated by their location in Antarctica and Greenland due to the different thicknesses and ages of the ice in the two continents. The zones are designated by a geographical label $L$ (henceforth referred to as geolabel), which are defined at each geographical coordinate (latitude, longitude) of the radar track. The geolabels are Greenland grounded ice (GGI), Greenland floating ice (GFI), Antarctica grounded ice (AGI), Antarctica floating ice (AFI), and Antarctica subglacial (ASG) lakes.

A useful approach to the design of RSs is based on evaluating the required SNR at the surface (referred here as SNR budget and represented by the notation SNR) that depends mainly on the instrument parameters and the orbit configuration. From the budget, the losses due to the target and the environment (subsurface reflectivity, attenuation rate, scattering losses, ionospheric distortions, and coherence losses) are excluded to determine the SNR margin available at the expected depth of the subsurface interface. This is justified on the basis of previous studies (see Section II-C). The SNR margin should be positive and higher than the sensitivity of the RS to detect the subsurface interface. To represent the range of possible values of the budget, we have considered $N_b$ different hypotheses of the SNR parameter, referred by the simulation index $b = 1, 2, \ldots, N_b$. The corresponding values of the budget parameter are denoted by the simulation index as the subscript, i.e., $\mathrm{SNR}_b$.

Next, starting from each of the airborne radargrams $P_{r,A}(r_A, c_A)$, the orbital radargrams $P^b_{r,E}(r_E, c_E)$ are simulated for $N_b$ different values of $\mathrm{SNR}_b$. The radargrams are 2-D matrices in which the rows ($r$) represent time samples of the received signal, and the columns ($c$) represent the frames acquired, while the RS moves in the along-track direction, and the values ($P_r$) in the matrix represent the received signal (which is a complex number, but, in this case, we convert it into the received power expressed in dB).

Each of the $N_b$ simulated radargrams is analyzed for assessing the orbital performance at two levels representing the primary and the secondary objectives of an orbital mission (see Section III-B). For the primary performance assessment, the IRHs and the basal interface are extracted from the simulated radargrams with the help of the ground truth available in the input airborne data. For the secondary performance assessment, we define and evaluate a metric that quantifies the interpretability of the detectable basal interface. This is achieved by applying an automatic subglacial lakes' detection algorithm [24] to the airborne and simulated radargrams, and comparing the accuracy of basal interface classification.

### D. Assumptions

In this article, we consider a VHF band orbital RS, with a central frequency of 45 MHz and a bandwidth of 10 MHz. The selected airborne RS operates at UHF frequencies with a central frequency of 195 MHz and a bandwidth of 30 MHz (see Table I). Note that the use of a UHF airborne RS (which depends on data availability) is detrimental to the estimation of performances of the considered orbital RS, as we can simulate the degradation of performance due to the minor bandwidth, but we cannot recover the advantages in terms of clutter and volume scattering at a lower frequency (see Appendices A and B for more details).

The proposed approach is based on the following assumptions.

*1) Frequency Dependence of Polar Ice Dielectric Properties:* For polar ice, the dielectric properties are affected by structural imperfections, the presence of impurities, and freezing/melting processes [47]. However, the real part of the permittivity has negligible variability with frequency, as reported in previous studies [47]–[49]. Using Debye equations, the real part is found to vary by less than $10^{-4}$% between the airborne and orbital frequencies. In contrast, the ice-sheet conductivity values are reported to have a spatially variable frequency dependence in Antarctica and Greenland [42], [49], which can be characterized by the Cole–Cole distribution parameter (see Section III-E and Appendix A). For simplicity, we assume a spatially homogeneous value of this parameter across Greenland and Antarctica. Depending on the availability of experimental data at different locations, the appropriate value of the Cole–Cole distribution parameter can be easily incorporated into the simulation chain.

*2) Range Dependence of Polar Ice Dielectric Properties:* Due to the heterogeneous nature of cryosphere targets, the dielectric profile changes with depth in a way that cannot be estimated easily. However, we assume that, for a small thickness (the order of a few resolution cells), the radar reflectivity is locally constant in the vertical direction [42]. This is generally true at RS wavelengths since the sensitivity of the RS to small changes in the dielectric profile depends on the bandwidth, which is relatively lower for long-wavelength RSs [48].

*3) Volume and Surface Scattering:* Volume scattering caused by distributed targets is assumed to be independent of the frequency (i.e., the volume scattering observed by the airborne RS is retained in the orbital radargrams). Thus, the volume scattering losses between 40 and 50 MHz are overestimated in the current approach (see Appendix A), and the real orbital RS will be subjected to much lower levels of these losses. Surface scattering in the simulated orbital radargrams (i.e., surface reflectivity) is assumed to be spatially invariable (−10 dB corresponding to Fresnel reflectivity at the ice–air interface).

*4) Other Performance-Limiting Factors:* The effects of clutter at the orbital footprint and the ionospheric distortions are not addressed by the simulations. These can be addressed in separate studies using well-established techniques [6], [30], and their effects can be mitigated. Nonetheless, we have considered the power loss due to the ionosphere in the definition of the SNR margin (see Appendix A) for the assessment of target detectability. Moreover, the difference in the antenna pattern between the airborne and orbital systems is not accounted for in the proposed approach.

*5) Effect of Processing:* The radar echo processing techniques applied to the airborne RS and possibly applicable to the orbital RS are likely to be different due to the differences in the acquisition scenarios. The simulations do not account for the differences in the echo processing techniques, except for the gain in orbital signal power due to range and along-track processing. The processing gains in the case of the airborne data are taken into account while normalizing the power with respect to the surface response.

*6) Geometric Losses:* In low-altitude airborne RS operating at UHF frequencies, the geometry (high dipping angles) of IRHs causes energy dispersion via several mechanisms, such as destructive stacking, SAR processing, and off-nadir ray path extension [50]. These losses are ignored in the proposed approach, which is constrained by the information available from the airborne data (i.e., the observed IRH reflectivity). The method only accounts for geometric losses resulting from the nadir distance between the interfaces and the platform. This assumption can result in an underestimation of the IRH and basal interface detection performance of the orbital RS, which does not suffer from these losses.

### *E. Orbital Data Simulation*

The simulation approach is based on reprocessing of available radargrams acquired over geological analogs of the investigated target [21]. This is done by identifying the differences in the analog and investigated acquisition scenarios (in terms of the instrument parameters, acquisition geometry, and target geoelectrical properties) and understanding the impact of these differences on the characteristics of the analog and investigated radargrams. In this article, the orbital radargrams are simulated using a special case of this analog-based simulation approach in which the analog and the investigated RSs acquire data over the same target (in this case, the polar ice regions). The advantage is that it is not necessary to assume the detailed geoelectrical models of the ice targets, and this also gives high structural fidelity between the analog and investigated target representation. However, the target attenuation factor depends on the central frequency of the RSs, which should be accounted for by processing the profile of the target radar response.

The simulation steps are briefly outlined as follows, where $z$ refers to the depth computed at each row index $r_A$ assuming a constant ice permittivity of 3.15, and $P_r$, $P_t$, $G^2$, $G_r$, $G_{\mathrm{az}}$, $\gamma_S$, $\gamma_{\mathrm{SS}}$, and $\rho$ are expressed in dB (refer to Nomenclature).

*1) Target Geoelectrical Modeling:* Considering the specular version of the radar equation (which assumes that the targets are flat and specular, their properties are constant over an area larger than the first Fresnel zone [51], [52], and the refraction gain is equal to 1), the airborne received power profile at the frame $c_A$ is given by

$$\begin{aligned} P_{r,A}(r_A, c_A) &= P_{t,A} + G_A^2 + G_{r,A} + G_{\mathrm{az},A} + \gamma_{S,A} \\ &\quad + \gamma_{\mathrm{SS},A}(z, c_A) - 10\log_{10}\left[\frac{64\pi^2\{H_A(c_A)+z\}^2}{\lambda_A^2}\right]. \end{aligned} \tag{1}$$

The power received from the surface, obtained by detecting the strongest reflection in each frame, represents the sample $z = 0$ in (1). Thus,

$$\begin{aligned} P_{r,A}(z=0, c_A) &= P_{t,A} + G_A^2 + G_{r,A} + G_{\mathrm{az},A} + \gamma_{S,A} \\ &\quad - 10\log_{10}\left[\frac{64\pi^2 H_A(c_A)^2}{\lambda_A^2}\right]. \end{aligned} \tag{2}$$

From (1) to (2), the subsurface target propagation factor of the airborne RS can be estimated by normalizing the frame power by the surface echo and removing the expected geometric losses

$$\begin{aligned} \gamma_{\mathrm{SS},A}(z, c_A) &= P_{r,A}(r_A, c_A) - P_{r,A}(z=0, c_A) \\ &\quad + 10\log_{10}\left[\frac{\{H_A(c_A)+z\}^2}{H_A(c_A)^2}\right]. \end{aligned} \tag{3}$$

The actual subsurface target propagation factor depends on the target reflectivity profile $\rho(z, c_A)$, the target-dependent attenuation $\alpha(z)$, and the central frequency $f_{c,A}$ of the airborne RS and is given by

$$\gamma_{\mathrm{SS},A}(z, c_A) = \rho(z, c_A) - \int_0^z f_{c,A}^{\eta}\alpha(z, c_A)dz \tag{4}$$

where $\eta$ is the Cole–Cole distribution parameter [42] that characterizes the frequency dependence of the englacial attenuation. $\eta = 0$ implies frequency independence, whereas $\eta = 1$ implies a strong linearly proportional frequency dependence of the radar attenuation in ice.

The reflectivity depends on the presence of discontinuities in the ice sheet (e.g., IRHs) at the scale of the RS wavelength. We assume that the medium between successive IRHs is homogeneous at the airborne frequency (therefore, it is also homogeneous at the orbital frequency, which is even lower), and the reflectivity is vertically uniform [42]. Thus, using (4), the integral term $\int_0^z f_{c,A}^{\eta}\alpha(z, c_A)dz$ is estimated as the local slope of the troughs in the $\gamma_{\mathrm{SS},A}(z, c_A)$ profile. Since the strong surface echo can mislead the slope estimation, we consider the profile starting from 100 m below the surface. This is justified because the attenuation within the surface layer is negligible due to very small values of the depth z compared to the deeper layers. In the top 100 m of the ice, we assume $\alpha = 0$. Since the central frequency is a constant in the integral, we can easily obtain $\int_0^z \alpha(z, c_A)dz$ by dividing the slope by $f_{c,A}^{\eta}$. The corresponding EORS target propagation factor $\gamma_{\mathrm{SS},E}(z, c_A)$ is given by

$$\begin{aligned} \gamma_{\mathrm{SS},E}(z, c_A) &= \gamma_{\mathrm{SS},A}(z, c_A) \\ &\quad - \left(f_{c,E}^{\eta} - f_{c,A}^{\eta}\right)\int_0^z \alpha(z, c_A)dz. \end{aligned} \tag{5}$$

Note that $\int_0^z \alpha(z, c_A)dz$ is positive. Therefore, (5) indicates that the orbital power decreases as the value of $\eta$ decreases since the orbital central frequency is lower than the airborne one.

*2) Signal Magnitude Correction:* Using radar equations (1) and (5), and the suitable orbital parameters that result in a given value of $\mathrm{SNR}_b$, the orbital received power $P^b_{r,E}(r_A, c_A)$ is calculated as

$$P^b_{r,E}(r_A, c_A) = P_{t,E} + G_E^2 + G_{r,E} + G_{\mathrm{az},E} + \gamma_{S,E} + \gamma_{\mathrm{SS},E}(z, c_A) - 10\log_{10}\left[\frac{64\pi^2(H_E+z)^2}{\lambda_E^2}\right] \quad (6)$$

where the surface reflectivity in the orbital case $\gamma_{S,E}$ is calculated from the dielectric permittivity at the ice–air interface and assumed to be $-10$ dB for all the simulations.

*3) Noise Correction:* This step considers the differences in the noise power level of the two scenarios due to the presence of different sources of noise. Note that, at airborne flying altitudes, the data are not affected by the galactic noise. On the contrary, sounding from a satellite platform is subjected to the isotropic cosmic microwave background (CMB). In this step, Rayleigh distributed galactic noise power [37], corresponding to an equivalent noise temperature at the orbital frequency and bandwidth, is stochastically added to the processed airborne radargrams.

*4) Bandwidth Correction:* The orbital bandwidth $B_E$ is typically lower than that of the airborne $B_A$ (as considered in this study). This difference is corrected by applying a low-pass filter to the processed airborne radargrams after the signal magnitude correction. Bandwidth correction ensures that the target reflectivity profile corresponds to the dielectric interfaces detectable with the bandwidth of the orbital RS.

*5) Range and Along-Track Sampling Correction:* The spacing between the samples in the range direction depends on the sampling frequency of the RSs. Similarly, the distance between successive pulses (frames of the radargrams) depends on the PRF of the RSs. These differences are addressed by appropriately resampling the radargram in range and along-track direction, using the nearest neighbor resampling technique. The details of the filtering and resampling process can be found in [21].

With these steps, we obtain the simulated radargram represented in terms of received power $P^b_{r,E}(r_E, c_E)$ for the design parameter $\mathrm{SNR}_b$.

### F. Primary Performance Assessment

*1) Automatic Extraction of the Prominent Dielectric Interfaces From Radargrams:* The dielectric interfaces representing the IRHs are known to have high reflectivity and a horizontal aspect. This information is well-known and used in the literature for automatic detection of the IRHs [53]–[55]. These techniques identify the IRHs based on their connectivity in the along-track direction and high contrast with respect to their neighboring range samples. We have adapted the state-of-the-art approaches [53] to formulate a computationally simple IRH detection algorithm applied to the airborne radargrams. The algorithm extracts horizontally connected linear features from the denoised radargram by wavelet decomposition. The extracted edges are refined by a morphological closing operation to eliminate isolated speckle reflections. The result is a binary IRH position mask matching the dimensions of the airborne radargram. It has a value of 1 at pixel positions where the IRHs have been identified in the airborne radargram and 0 elsewhere. Due to possible artifacts caused by the strong surface and basal interface reflections in the simulated radargrams, the mask considers only the region from 100 m below the surface to 100 m above the basal interface.

The basal interface is the deepest reflecting horizon in the radargram having a significantly high intensity (due to high dielectric contrast) and a horizontal continuity with its along-track neighboring samples. This knowledge has been used for the automatic detection of the basal interface from the radargrams following the techniques described in [56] and [57]. The output of the automatic detection is a binary basal interface position mask matching the dimensions of the airborne radargram. It has a value of 1 at positions where the basal interface has been identified in the airborne radargram and 0 elsewhere.

*2) Definition of the Primary Performance Metrics:* In the next step, we define metrics to quantify the detectability of the prominent interfaces in the $b$th simulated radargram against the galactic noise level. For this step, the reference ground truth is taken as the IRH and basal interface position masks derived from the input airborne data (this is valid since the data quality, and therefore the detection performance of the airborne, is higher than the orbital and has been validated in the literature). The mask is first resampled to the dimensions of the simulated radargrams (in terms of range resolution, sampling frequency, and along-track sampling) to achieve a pixel-to-pixel correspondence.

The evaluation of the IRH detection metric consists of checking the SNR in the simulated radargram at the positions given by the IRH reference ground truth. First, the resampled IRH position mask is compared pixel-by-pixel to the simulated radargram to create a binary map of the detectable IRHs. The map has a value of 1 at positions for which the mask is 1, and the simulated SNR ($P^b_{r,E} - 10\log_{10}[kB_E T_{\mathrm{cmb}}]$) is above the SNR margin and has 0 elsewhere. Next, we estimate the ratio of the total number of detectable IRHs in the map to the total number in the IRH position mask for each frame $c_E$ of the $b$th simulated radargram. The ratio, thus, obtained is defined as the IRH detection performance metric $\theta_b(c_E)$, i.e., the probability of IRH detection in the frame $c_E$.

Similarly, the basal interface position mask is compared pixel-by-pixel with the $b$th simulated radargram to create the basal interface detection metric $\beta_b(c_E)$, defined for each frame $c_E$. The metric is $\beta_b(c_E) = \mathrm{NULL}$ for the frames for which the mask is 0 at every sample, representing the case where the basal interface is not detectable in the airborne data and, hence, definitely not present in the simulated data (the simulation process cannot create information that is absent in the input airborne data). At the pixel positions where mask $=$ 1, the metric is $\beta_b(c_E) = 1$ if the simulated SNR is above the SNR margin (representing the cases of the detectable basal interface in the simulated data), while $\beta_b(c_E) = 0$ if the simulated SNR is below the SNR margin (representing the cases of nondetectability of the basal interface in the simulated data).

Note that the noise power level is implicit in the SNR evaluation from the received EORS power. Hence, the simulated radargrams used for extracting the IRH and basal performance metrics do not include the Noise Correction processing step. If the noise corrected radargrams are used for IRH and basal performance analysis, they can lead to overestimation of the performance due to the stochastic nature of noise. The high levels of noise can be falsely identified as detectable IRHs or basal reflections, which is purely due to the simulation process (thus, this does not represent the real scenario).

*3) Projection of the Performance Onto the Parameter Space:* Next, the performance metrics are grouped by the geolabels. For the frames $c_E^L$ having the same geolabel $L$, we define the cumulative fraction of frames $\chi_b^L(\theta)$ for which the IRH detection metric $\theta_b(c_E)$ is greater than a probability threshold $\theta \in [0, 1]$

$$\chi_b^L(\theta) = \frac{\text{count}\left[\theta_b\left(c_E^L\right) \geq \theta\right]}{N_E^L}. \quad (7)$$

The plot of $\chi_b^L$ versus $\theta$ can be understood as a cumulative distribution of IRH detection performance for each geolabel and each simulated radargram. For interpreting the performance and supporting the design, the information from the cumulative plots is projected onto the parameter space defined by the target and the instrument parameters. This can be done by knowing the requirement on the probability threshold $\theta$ and the cumulative performance $\chi_b^L(\theta)$ that should be satisfied by the design. These are defined in terms of the minimum required per-frame probability of IRH detection $\theta_{\min}^L$ and the minimum required cumulative fraction of frames $\chi_{\min}^L$. The superscript $L$ denotes that these requirements may be different for different geolabels. The minimum required SNR for the detectability of the IRHs in the zone $L$ is given by the smallest value of $\text{SNR}_b$ such that at least $\chi_{\min}^L$ frames have more than $\theta_{\min}^L$ IRHs detectable per frame

$$\text{SNR}_{\min}\left(\theta_{\min}^L, \chi_{\min}^L, L\right) = \min_{\forall b}\left\{\text{SNR}_b : \chi_b^L\left(\theta_{\min}^L\right) \geq \chi_{\min}^L\right\}. \quad (8)$$

However, the orbital instrument should be designed for a single value of SNR that should satisfy the detection requirements across all the geolabels. For a set of requirements $(\theta_{\min}^L, \chi_{\min}^L)$, the best design parameter $\text{SNR}_{\text{design}}$ is given by

$$\text{SNR}_{\text{design}} = \max_{\forall L}\left\{\text{SNR}_{\min}\left(\theta_{\min}^L, \chi_{\min}^L, L\right)\right\}. \quad (9)$$

In a more straightforward approach, the values of the basal interface detection $\beta_b(c_E)$ are grouped for the frames $c_E^L$ having the same geolabels. The grouped performance is estimated as the fraction of frames $\beta_b^L$ for which the basal interface detection metric is equal to 1 and is given by

$$\beta_b^L = \frac{\text{count}\left[\beta_b\left(c_E^L\right) = 1\right]}{\text{count}\left[\left\{\beta_b\left(c_E^L\right) = 1\right\} \vee \left\{\beta_b\left(c_E^L\right) = 0\right\}\right]}. \quad (10)$$

For a mission requirement of $\beta_{\min}^L$ on the basal interface detectability for the geographical zone $L$, the minimum required SNR is given by the smallest value of $\text{SNR}_b$ such that at least $\beta_{\min}^L$ frames have a detectable basal interface

$$\text{SNR}_{\min}\left(\beta_{\min}^L, L\right) = \min_{\forall b}\left\{\text{SNR}_b : \beta_b^L \geq \beta_{\min}^L\right\}. \quad (11)$$

The design SNR is obtained similar to (9), as the maximum value of $\text{SNR}_{\min}$ satisfies the requirement in all the zones.

### G. Secondary Performance Assessment

*1) Characterization of the Nature of the Basal Interface:* For the secondary performance assessment, we focus on the ability to characterize a crucial basal boundary condition, i.e., the presence of subglacial lakes. It is obvious that the secondary performance is analyzed only for frames for which the primary performance is satisfied, i.e., the basal interface is detectable in the orbital data. To detect subglacial lakes, we consider the automatic algorithm proposed in [24] for analyzing airborne radargrams and adapt it to the case of orbital data. The algorithm exploits the extreme differences in the properties of the basal interface waveforms (set of range samples centered around the basal reflection in each frame) depending on its constituent materials, namely, ice–bedrock or ice–water (i.e., subglacial lake).

For each pixel of the basal interface, considering these properties, a set of eight features are extracted that model the basal interface topography (root mean square height and the local waveform correlation), the shape of the waveforms (leading and the trailing edge steepness), and the statistical properties (mean adjusted basal peak power, the coefficient of variation, the skewness, and the kurtosis). These features are extracted and normalized for each frame in which the basal interface is detected, and analyzed by an SVM classifier with a radial basis function (RBF) kernel to discriminate between samples related to the presence $n_+$ or the absence $n_-$ of subglacial lakes.

The algorithm [24] is applied to the airborne and the corresponding simulated radargrams. Training is performed using 25% randomly picked samples from those labeled lake $n_+$ and not-lake $n_-$, and cross-validation using the remaining 75% of the samples. A balanced training set is created comprising equal proportions of lake $n_+$ and not-lake $n_-$ samples. The classification performance is expressed in terms of overall accuracy, precision, specificity, and recall (also called hit rate) for the orbital data and the airborne data. The specificity is computed as = 100—false alarm rate, while the recall = 100—miss rate.

*2) Subglacial Lakes' Detection Metric:* Next, we define the lake detection performance metric as a vector $\Lambda_b(c_E)$ defined for each frame of the $b$th simulated radargram. The metric is evaluated as follows: 1) the trained SVM classifier is separately applied to the airborne and simulated orbital radargrams to obtain two vectors $\ell_{\text{ARS}}$ and $\ell_{\text{EORS}}$ of the predicted labels of the basal interface (i.e., $n_+$ lake and $n_-$ nonlake); 2) the vector of the ARS predicted labels $\ell_{\text{ARS}}$ is resampled to match the along-track resolution of the orbital, to have a one-to-one correspondence between the two vectors; and 3) for both the ARS and the EORS predicted labels, we compute the vectors representing correct prediction, i.e., $\xi_{\text{ARS}}$ and $\xi_{\text{EORS}}$ as follows:

$$\xi_i = \begin{cases} 1, & \text{if } \ell_i = \text{GT}_i \\ 0, & \text{otherwise} \end{cases} \quad (12)$$

where $\text{GT}_i$ indicates the ground truth and the index $i$ indicates $i$ = EORS, ARS. Hence, vectors $\xi_{\text{ARS}}$ and $\xi_{\text{EORS}}$ are equal to 1 when the label is correctly predicted, whereas it is equal to 0 if the prediction is incorrect; and 4)we define $\Lambda(c_E)$ by comparing the vectors $\xi_{\text{ARS}}$ and $\xi_{\text{EORS}}$ as follows:

$$\Lambda(c_E) = \begin{cases} 0, & \text{if } \beta_b(c_E) = 0 \\ 1, & \text{if } \xi_{\text{ARS}} = 0 \wedge \xi_{\text{EORS}} = 0 \\ 2, & \text{if } \xi_{\text{ARS}} = 0 \wedge \xi_{\text{EORS}} = 1 \\ 3, & \text{if } \xi_{\text{ARS}} = 1 \wedge \xi_{\text{EORS}} = 0 \\ 4, & \text{if } \xi_{\text{ARS}} = 1 \wedge \xi_{\text{EORS}} = 1. \end{cases} \tag{13}$$

## IV. Experimental Results

### A. Definition of the Dataset

Based on the significant advantages of a 45-MHz sounder (see Section II) with respect to the other cases presented in the literature, we consider an orbital RS with parameters similar to the one proposed in [12] and [14]. The airborne radargrams are taken from the database provided by the Centre for Remote Sensing of the Ice-Sheets (CReSIS), acquired by the airborne multichannel coherent radar sounder (MCoRDS) [1]. The details of the selected campaigns and flight lines are 2017_Greenland_P3 (0328_01, 0410_03, 0413_01, 0502_01, 0505_01, 0412_01, 0511_01); 2017_Antarctica_P3 (1125_03, 1116_03, 1112_03, 1124_03, 1103_05); 2013_Antarctica_P3 (1120_01, 1119_01, 1126_01, 1127_01); and 2016_Antarctica_DC8 (1115_03, 1115_04, 1103_06).

Table I lists the parameters of the airborne and the proposed orbital systems. The input radargrams are processed with the range and azimuth compression, and the minimum variance distortionless response (MVDR) algorithm [26], [58]. The MVDR algorithm mitigates clutter and noise in the data with better performance than other techniques, which helps in the primary performance assessment by reducing misclassification of clutter as subsurface reflectors. Moreover, the algorithm in [24] used for the secondary performance assessment is also based on MVDR-processed data. However, the MVDR processing suffers from a self-nulling problem that is related to the suppression of very strong signals relative to the noise [26], [58].

The Cole–Cole distribution parameter $\eta$, henceforth referred to as frequency-dependence factor, is expected to have high spatial variability. For simplicity, we have considered a constant value of 0.08 [42], [59] for Greenland and 0.18 [42], [60] for Antarctica simulations. The sensitivity of the proposed approach to the uncertainties in the value of $\eta$ has been discussed in Appendix B-B.

The SNR budget at the surface (which is considered as the main variable for the design of the system) is given by

$$\begin{aligned} \text{SNR}_b = P_t + G^2 + \gamma_S + G_r + G_{\text{az}} \\ + 10\log_{10}\left[\frac{\lambda^2}{64\pi^2 H^2 k B T_{\text{cmb}}}\right] \end{aligned} \tag{14}$$

where $k$ is the Boltzmann's constant and the other symbols are described in Table I. In this experiment, we consider six different values of the SNR budget at the surface $\text{SNR}_b = \{65, 70, 75, 80, 85, 90\}$ dB. For considering the subsurface reflector to be detectable, the SNR margin at the subsurface is taken to be 5 dB, accounting for ionospheric and coherence losses. Justification of the value of the SNR margin is provided in Appendix A.

TABLE I
Proposed Orbital [12] and Airborne MCoRDS [1] Parameters

| **Parameter** | **MCoRDS (ARS)** | **EORS** |
|---|---|---|
| Central frequency $f_c$ (MHz) | 195* | 45* |
| Wavelength $\lambda$ (m) | 1.54 | 6.66 |
| Galactic noise temperature $T_{cmb}$ (K) [37] | - | 6320 |
| Bandwidth $B$ (MHz) | 30 | 10 |
| Altitude $H$ (km) | 2 - 4 | 500 |
| Along-track resolution (m) | 300 | 30 |
| Sampling frequency (MHz) | 45 | 12 |
| Transmitted power $P_t$ (dB) | 30.21 | 23 - 29 |
| Pulse length $\tau$ ($\mu s$) | 10 | 100 |
| Range processing gain $G_r = \tau B$ (dB) | 24.77 | 30 |
| Pulse-repetition frequency $PRF$ (Hz) | 343 | 1200 |
| Platform velocity $vel$ (m/s) | 144 | 7616 |
| Along-track processing gain $G_{az} = \sqrt{\frac{\lambda H}{2}\frac{PRF}{vel}}$ (dB) | 16 | 23 |
| Two-way antenna gain $G^2$ (dB) | 6 | 4 - 20 |
| Surface reflectivity $\gamma_S$ (dB) | -10 | |
| SNR budget at surface $SNR_b$ (dB) | 107.6 | 65 - 90 |

* These are the parameters for the MCoRDS-3 instrument in the following of the considered campaigns: 2017_Greenland_P3, 2017_Antarctica_P3, 2013_Antarctica_P3. For the flight lines from the 2016_Antarctica_DC8 campaign, the central frequency is 190 MHz with a bandwidth of 50 MHz.

The five geolabels $L$ are determined with the help of several ancillary datasets available for the earth's polar regions. For Greenland, the MEaSURE's Greenland Ice Mapping Project (GIMP) ice, ocean, and grounded-ice masks [61] are used to obtain the labels for grounded ice $L =$ GGI and floating ice $L =$ GFI in Greenland. For Antarctica, the Norwegian Polar Institute's Quantarctica package [62] is used to identify the grounded ice $L =$ AGI and the floating ice $L =$ AFI from the boundaries dataset [63], [64]. The subglacial lakes $L =$ ASG are analyzed within the Lake District of East Antarctica and Siple Coast. They are labeled using the radar-detected lakes [65] in the subglacial lakes inventory [66], [67] and the demarcated boundary of the Vostok lake [68] (present along the East Antarctica radar track). As in [24], a subset of these labels is also used as ground truth for the secondary

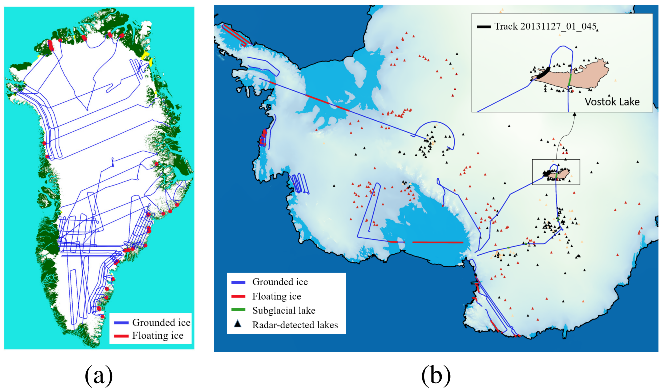


Fig. 3. Selected airborne radargram tracks and related geolabels: (a) in Greenland and (b) in Antarctica. The black triangles in (b) indicate radar-detected lakes [65], [66], which were used to generate the geolabels for the subglacial lakes. The inset map shows the location of the track corresponding to Fig. 4.

performance assessment. Fig. 3 shows the track locations of the input airborne data along with their geolabels. The selected airborne dataset covers a track of 1 08 000 km, of which about 99 000 km are expected to have a detectable basal interface in the airborne data.

In the following, we present the experimental results obtained by applying the proposed approach to the selected set of airborne radargrams. First, we show some examples of simulated orbital radargrams. Next, we present the results of the primary performance assessment for the detection of the IRHs and the basal interface. Finally, we report the secondary performance analysis related to the characterization of the basal interface, in terms of classification accuracy of subglacial lakes.

### *B. Simulated Orbital Radargrams*

Fig. 4(a) shows an example of the average received power profile of the simulated orbital and the airborne frames for a radargram acquired over the Vostok lake in East Antarctica. The effect of the signal magnitude correction step is visible from the different slopes of the received power profile for the two different RS frequencies. Furthermore, the effect of noise correction resulting in the noise floor nearly matching the cosmic noise level can also be observed. Fig. 4(b)–(d) shows examples of the input airborne radargram and the simulated radargrams for two extreme values of the SNR budget. Visually, we can see that increasing the SNR budget increases the detectability of the IRH and the basal interface. Another observation is the reduction in the range resolution due to a lower bandwidth of the orbital RS. This results in a reduced spatial sampling of the detectable IRHs in the simulated radargrams.

### *C. IRH Detection Performance*

Fig. 5(a)–(e) shows the cumulative distribution of the IRH detection performance for each geolabel $L$. The horizontal axis shows the probability $\theta$, while the vertical axis shows the cumulative fraction of frames $\chi_b^L(\theta)$ having IRH detection greater than $\theta$. We see that the distribution shifts toward the top right corner by increasing the SNR budget, indicating

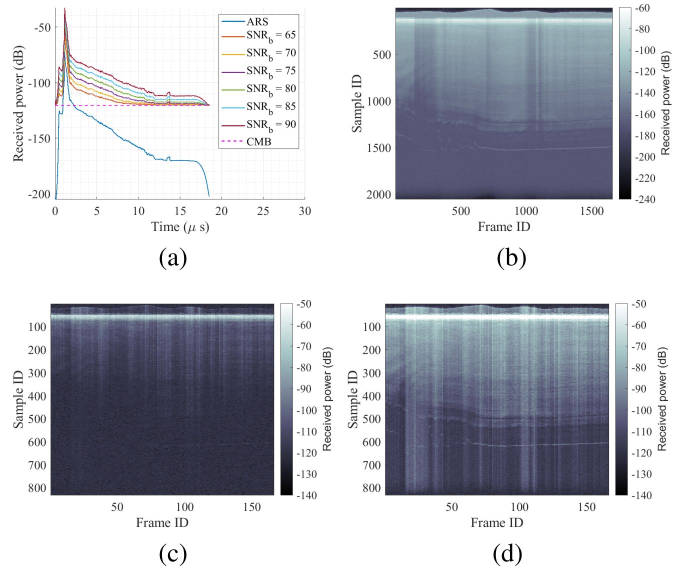


Fig. 4. Examples of simulated radargrams and average received power profile corresponding to the airborne radargram 20131127_01_045 in East Antarctica. (a) Average frame power of the airborne and the simulated orbital radargrams for different SNR$_b$ values, (b) airborne radargram, (c) simulated orbital radargram for SNR$_b$ = 65 dB, and (d) simulated orbital radargram for SNR$_b$ = 90 dB. The location of the track is shown in the inset map in Fig. 3. Note that $\eta = 0.18$ for this simulation.

an improvement in the grouped IRH detection performance (i.e., a higher number of frames has a higher IRH detection metric). Furthermore, the plots reveal that the IRH occurring in the floating ice in Greenland and Antarctica has a better detection performance compared to the grounded ice and subglacial lakes. An example of projecting the performance onto the parameter space is demonstrated here, considering the requirements $\theta_{\min}^L = 0.70$ and $\chi_{\min}^L = 0.70$ for all $L$. These requirements are indicated by the red vertical lines and the magenta dashed horizontal lines, respectively, in Fig. 5(a)–(e). For ease of understanding, the region of the cumulative distribution satisfying these two conditions is marked by a green box. For each geolabel, the plots occurring within the green box represent the required SNR$_b$ values. For example, for the ASG lakes, the green box contains the plots corresponding to SNR$_b$ $\geq$ 80 dB. Therefore, for this zone, the minimum required SNR budget is $\text{SNR}_{\min}(0.70, 0.70, L = \text{ASG}) = 80$ dB. Similarly, by analyzing all the zones, we obtain the projection of the geolabels versus the required SNR budget shown by the yellow bars in Fig. 5(f). From this graph, we can see that the design SNR budget that satisfies the detectability of IRHs in all the five geographical zones for the given set of requirements is $\text{SNR}_{\text{design}} = 85$ dB (indicated by the red dashed vertical line).

The mission requirements typically flow down from the scientific goals of the mission and may be different for different geographical zones. However, due to the absence of a well-defined orbital mission and avoid introducing any bias due to subjective assumptions, we evaluate the design SNR for the full range of the mission requirements and also consider them to be independent of the geolabels. Fig. 6 tabulates the

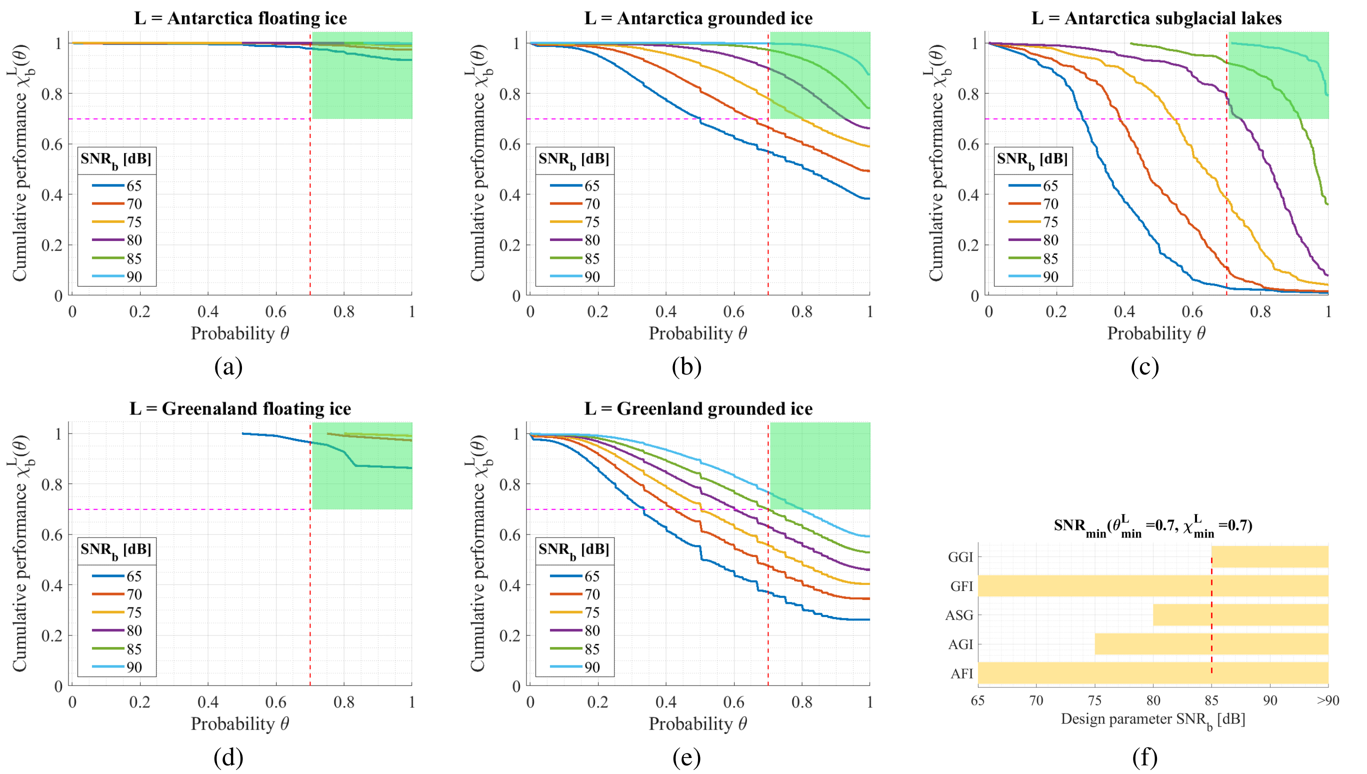


Fig. 5. Results of the IRH detection performance for different geolabels and SNR$_b$'s. Cumulative distribution of the IRH detection performance for (a) AFI, (b) AGI, (c) ASG lakes, (d) GFI, and (e) GGI. An example of the SNR budget selection based on a possible set of mission requirements is presented in (f). It shows the value of SNR$_b$ that gives the per-frame IRH detection probability $\theta$ greater than 0.70 (red dashed vertical line in (a)–(e), which is satisfied by at least 70% of all the frames (magenta dashed horizontal line in (a)–(e)]. The regions of the cumulative distribution plots that satisfy these requirements are highlighted in the green box. The corresponding minimum required SNR$_b$ values for detectability in each zone are indicated by the yellow bars in (f). The red dashed vertical line in (f) corresponding to SNR$_b$ = 85 dB indicates the design SNR budget necessary for satisfying the IRH detection requirements for all the five geolabels.

| Requirement on Probability of IRH detection per frame \ Requirement on Cumulative fraction of frames | 0.00 | 0.05 | 0.10 | 0.15 | 0.20 | 0.25 | 0.30 | 0.35 | 0.40 | 0.45 | 0.50 | 0.55 | 0.60 | 0.65 | 0.70 | 0.75 | 0.80 | 0.85 | 0.90 | 0.95 | 1.00 |
|---|---|---|---|---|---|---|---|---|---|---|---|---|---|---|---|---|---|---|---|---|---|
| 1.00 | 65 | >90 | >90 | >90 | >90 | >90 | >90 | >90 | >90 | >90 | >90 | >90 | >90 | >90 | >90 | >90 | >90 | >90 | >90 | >90 | >90 |
| 0.95 | 65 | 65 | 65 | 75 | 75 | 85 | 90 | 90 | >90 | >90 | >90 | >90 | >90 | >90 | >90 | >90 | >90 | >90 | >90 | >90 | >90 |
| 0.90 | 65 | 65 | 65 | 65 | 70 | 75 | 80 | 85 | 90 | 90 | >90 | >90 | >90 | >90 | >90 | >90 | >90 | >90 | >90 | >90 | >90 |
| 0.85 | 65 | 65 | 65 | 65 | 65 | 70 | 75 | 80 | 85 | 85 | 90 | 90 | >90 | >90 | >90 | >90 | >90 | >90 | >90 | >90 | >90 |
| 0.80 | 65 | 65 | 65 | 65 | 65 | 70 | 70 | 75 | 80 | 80 | 85 | 85 | 90 | 90 | >90 | >90 | >90 | >90 | >90 | >90 | >90 |
| 0.75 | 65 | 65 | 65 | 65 | 65 | 65 | 70 | 70 | 75 | 80 | 80 | 85 | 85 | 90 | 90 | >90 | >90 | >90 | >90 | >90 | >90 |
| 0.70 | 65 | 65 | 65 | 65 | 65 | 65 | 70 | 70 | 75 | 75 | 75 | 80 | 80 | 85 | 85 | 90 | 90 | >90 | >90 | >90 | >90 |
| 0.65 | 65 | 65 | 65 | 65 | 65 | 65 | 70 | 70 | 70 | 75 | 75 | 75 | 80 | 80 | 85 | 85 | 90 | 90 | >90 | >90 | >90 |
| 0.60 | 65 | 65 | 65 | 65 | 65 | 65 | 65 | 70 | 70 | 75 | 75 | 75 | 80 | 80 | 80 | 80 | 85 | 90 | 90 | 90 | >90 |
| 0.55 | 65 | 65 | 65 | 65 | 65 | 65 | 65 | 70 | 70 | 75 | 75 | 75 | 75 | 80 | 80 | 80 | 80 | 85 | 85 | 90 | 90 |
| 0.50 | 65 | 65 | 65 | 65 | 65 | 65 | 65 | 70 | 70 | 70 | 75 | 75 | 75 | 80 | 80 | 80 | 80 | 85 | 85 | 85 | 90 |
| 0.45 | 65 | 65 | 65 | 65 | 65 | 65 | 65 | 65 | 70 | 70 | 75 | 75 | 75 | 75 | 80 | 80 | 80 | 85 | 85 | 85 | 90 |
| 0.40 | 65 | 65 | 65 | 65 | 65 | 65 | 65 | 65 | 70 | 70 | 70 | 75 | 75 | 75 | 80 | 80 | 80 | 80 | 85 | 85 | 90 |
| 0.35 | 65 | 65 | 65 | 65 | 65 | 65 | 65 | 65 | 65 | 70 | 70 | 70 | 75 | 75 | 75 | 80 | 80 | 80 | 85 | 85 | 85 |
| 0.30 | 65 | 65 | 65 | 65 | 65 | 65 | 65 | 65 | 65 | 70 | 70 | 70 | 75 | 75 | 75 | 80 | 80 | 80 | 85 | 85 | 85 |
| 0.25 | 65 | 65 | 65 | 65 | 65 | 65 | 65 | 65 | 65 | 65 | 70 | 70 | 70 | 75 | 75 | 75 | 80 | 80 | 80 | 85 | 85 |
| 0.20 | 65 | 65 | 65 | 65 | 65 | 65 | 65 | 65 | 65 | 65 | 65 | 70 | 70 | 75 | 75 | 75 | 80 | 80 | 80 | 85 | 85 |
| 0.15 | 65 | 65 | 65 | 65 | 65 | 65 | 65 | 65 | 65 | 65 | 65 | 70 | 70 | 70 | 75 | 75 | 75 | 80 | 80 | 80 | 85 |
| 0.10 | 65 | 65 | 65 | 65 | 65 | 65 | 65 | 65 | 65 | 65 | 65 | 65 | 70 | 70 | 70 | 75 | 75 | 80 | 80 | 80 | 85 |
| 0.05 | 65 | 65 | 65 | 65 | 65 | 65 | 65 | 65 | 65 | 65 | 65 | 65 | 65 | 70 | 70 | 70 | 75 | 75 | 75 | 80 | 80 |
| 0.00 | 65 | 65 | 65 | 65 | 65 | 65 | 65 | 65 | 65 | 65 | 65 | 65 | 65 | 65 | 65 | 65 | 65 | 65 | 65 | 65 | 65 |

Fig. 6. SNR values for detectability in all the five zones for different sets of mission requirements on the probability of IRH detection and the cumulative fraction of frames. The red box identifies the scenario shown in Fig. 5. The values in the matrix indicate the minimal value of SNR$_b$ that satisfies the requirements in the corresponding row and column headings.

design SNR budget that satisfies the detectability in all zones computed for the full range of possible $\theta_{\min}$ and $\chi_{\min}$.

Depending on the scientific objectives of the mission and the feasibility of obtaining the desired $SNR$, a tradeoff between the requirements and the instrument design should be identified. Let us illustrate how the performance projection supports this tradeoff analysis. From the cumulative distribution plots (see Fig. 5), we see that, for the floating ice in Antarctica, even with SNR$_b$ = 65 dB, very high IRH detection performance is obtained (more than 95% of the IRHs are detectable in more than 90% of the frames). For the floating ice in Greenland, this is the case for SNR$_b$ $\geq$ 70 dB. The IRHs in the interior of the ice sheets are relatively more difficult to detect. To detect more than 70% of the IRHs in the grounded ice in Antarctica, SNR$_b$ $\geq$ 75 dB is required, whereas, over the subglacial lakes, this requirement is even higher (SNR$_b$ $\geq$ 80 dB). Moreover, the IRH detectability is highly sensitive to the SNR$_b$ values for the ASG zone, ranging from probability of detection smaller than 0.3 for SNR$_b$ = 65 dB to one larger than 0.9 for SNR$_b$ = 90 dB. The most critical targets appear to be the IRHs in the grounded ice in Greenland, which requires at least 90-dB SNR to detect more than 70% of the layers.

Considering the same requirements for all geolabels, the values of the design SNR shown in Fig. 6 are likely to be affected by the interior of the ice sheets (AGI, GGI, and ASG). Besides design and performance assessment, such tradeoff analysis combined with the study on the scientific interests in each zone can also be used to define the feasible IRH detection requirements for each geographical zone.

TABLE II
BASAL INTERFACE DETECTION PERFORMANCE FOR DIFFERENT GEOGRAPHICAL ZONES (REPORTED AS PERCENTAGE)

| | **Design parameter $SNR_b$ [dB]** | | | | | |
|---|---|---|---|---|---|---|
| $L$ | **65** | **70** | **75** | **80** | **85** | **90** |
| AFI | 99.7 | 99.7 | 99.8 | 99.8 | 99.8 | 99.8 |
| AGI | 66.4 | 77.2 | 86.5 | 93.2 | 97.2 | 99.1 |
| ASG | 40.6 | 70.3 | 92.7 | 98.4 | 99.5 | 100 |
| GFI | 99.4 | 99.4 | 99.4 | 99.4 | 99.4 | 99.4 |
| GGI | 26.1 | 33.8 | 43.5 | 53.0 | 61.4 | 69.7 |

### *D. Basal Interface Detection Performance*

Table II shows the performance projection of the basal interface detection for each geographical zone and SNR budget. The reported values represent the grouped performance metric ($\beta_b^L$), which denotes the percentage of frames having a detectable basal interface in the simulated radargrams. As an example of the selection of the design SNR, let us consider a basal interface detection requirement of $\beta_{\min}^L = 60\%$ for all zones. With a design SNR budget of 85 dB, this requirement is satisfied in all five zones.

The table can be used for a tradeoff analysis similar to that described for IRH detection performance. Similar to the IRH detection, the highest basal interface detectability is seen for the floating ice. These are shallow targets with high interface reflectivity (ice–water dielectric discontinuity) and, thus, have a very high basal interface detection performance, even with low SNR values. In the subglacial lakes zone, an SNR higher than 75 dB is required to penetrate up to the basal interface of more than 90% of the frames. However, due to the strong reflectivity of the ice–water interface, nearly all the basal interfaces can be detected when $\mathrm{SNR}_b \geq 80$ dB. The grounded ice in Greenland is a critical target for basal interface detection, especially at low values of $\mathrm{SNR}_b$ as also observed with the IRH performance. A plausible explanation can be the value of the frequency-dependence factor considered for the simulations. As shown in Appendix B-B, incorrect lower values of $\eta$ can result in underestimation of the detection performance.

### *E. Subglacial Lakes' Detection Performance*

We illustrate the subglacial lakes performance considering two cases: case (i) $\mathrm{SNR}_b = 85$ dB and case (ii) $\mathrm{SNR}_b = 90$ dB, where the basal interface detection metric is more than 99%. To determine the kernel parameters of the SVM classifier, we apply a tenfold cross-validation considering the range of the parameters $c \in [1, 2^{20}]$ and $\gamma \in [2^{-2}, 2^4]$. In the cross-validation, for each value of $c$ and $\gamma$, the training samples are divided in $k = 10$ folds, and an SVM model is trained with $c$ and $k-1$ folds. Each SVM model is then validated on the remaining sample fold, considering the accuracy as a metric. The validation accuracy is averaged over the $k$ experiments. Finally, the best values of $c$ and $\gamma$ are defined as those maximizing the average accuracy. The optimal kernel parameters are $c = 2^{20}$ and $\gamma = 8$ for both cases (i) and (ii). Table III shows the classification performance for the airborne [24] data and for the orbital data for cases (i) and (ii). For both cases, the accuracy is higher than 98.5% and comparable to that obtained from the ARS data. Also, the other classification performances (specificity, precision, and recall) have high values, confirming the possibility of detecting subglacial lakes from the orbital data with high performance. The difference in the classification performance of cases (i) and (ii) is extremely small, indicating that, if the basal interface is detectable, it is possible to analyze the nature of the interface and detect the presence of subglacial lakes.

TABLE III
CLASSIFICATION PERFORMANCE OF THE SUBGLACIAL LAKE DETECTION ALGORITHM APPLIED TO THE AIRBORNE DATA AND THE ORBITAL DATA FOR THE CASE (i) $\mathrm{SNR}_b = 85$ dB and Case (ii) $\mathrm{SNR}_b = 90$ dB

| | **ARS [24]** | **Case (i)** | **Case (ii)** |
|---|---|---|---|
| Recall | 99.08 | 99.89 | 99.88 |
| Specificity | 99.08 | 97.21 | 99.96 |
| Precision | 99.28 | 97.38 | 99.81 |
| **Overall Accuracy** | 98.22 | 98.63 | 99.92 |

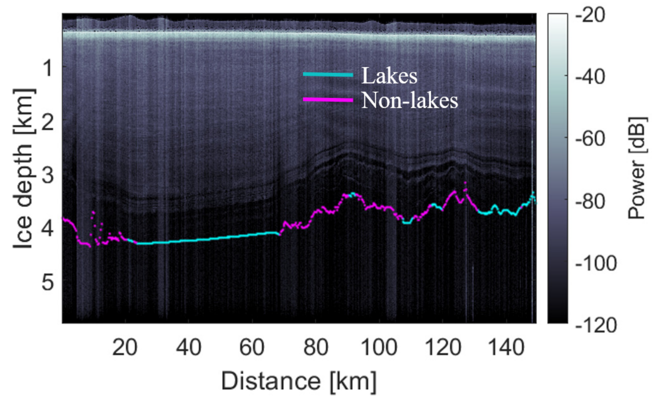


Fig. 7. Results of the automatic lakes' detection algorithm applied to simulated orbital radargram corresponding to $\mathrm{SNR}_b = 90$ dB and for the radar track 20131127_01_045-047 in East Antarctica containing the Vostok lake. The blue region of the basal interface is detected as lake while the magenta region is detected as nonlake.

Fig. 7 shows a simulated orbital radargram corresponding to $\mathrm{SNR}_b = 90$ dB and the predicted labels of the basal interface. In this radargram, the Vostok lake, which appears as a continuous flat reflector (indicated in blue), is detected by the algorithm and well discriminated from the surrounding bedrock samples (indicated in magenta). Fig. 8 shows the lake detection metric for $\mathrm{SNR}_b = 90$ dB, plotted along the radar tracks in the Lake District of Antarctica. From the map, it is evident that the algorithm effectively classifies the basal interface into lakes and nonlakes for a major part of the track (marked in green) for both the airborne and the orbital. The basal interface around the margins of the Vostok lake is misclassified (marked in red) in both the airborne and the orbital radargrams. However, there are a few locations where

This article has been accepted for inclusion in a future issue of this journal. Content is final as presented, with the exception of pagination.



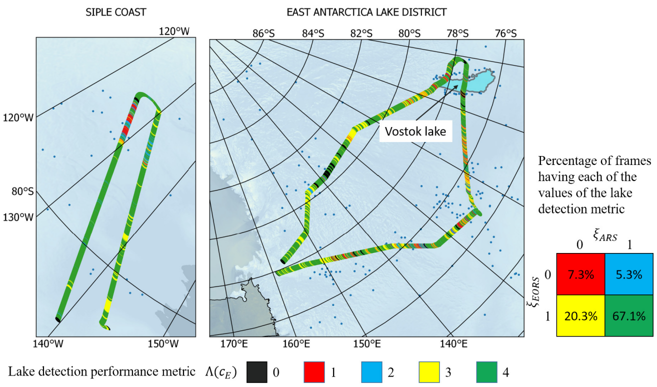


Fig. 8. Lakes' detection performance metric $\Lambda(c_E)$ plotted along the radar track in Antarctica Lake district and Siple Coast. The metric values indicate locations for which the basal interface is: not detectable (0); not correctly classified in both the airborne and the simulated orbital radargrams (1); correctly classified in the airborne but not in the orbital ones (2); correctly classified in the orbital but not in the airborne ones (3); and correctly classified in both the airborne and the simulated orbital radargrams (4). The matrix on the right shows the percentage of frames for each of the metric values.

the classification is accurate for the airborne and not for the orbital (yellow) and vice versa (blue).

## V. Discussion and Conclusion

In this article, we have presented a methodology for a detailed and realistic assessment of the performance of an orbital RS in detecting important scientific targets in the polar ice subsurface. The performance assessment methodology is based on simulating the orbital radargrams, starting from the available databases of airborne radargrams and evaluating a set of performance metrics defined in this article. The orbital radargrams are simulated corresponding to different values of the SNR budget at the surface, and the performance analysis of the simulated radargrams is used to reveal the SNR budget that maximizes the detectability of the targets across different geographical regions of the polar cryosphere. A hierarchical approach is used to evaluate the detection performance of: 1) IRHs; 2) basal interface; and 3) subglacial lakes.

The methodology, in general, has been demonstrated on an orbital RS with a carrier of 45 MHz and a bandwidth of 10 MHz, by simulating the radargrams starting from data acquired by MCoRDS (operating in the UHF band). The results indicate that the SNR budget required to detect IRHs and the basal interface varies across different geographical zones. Detection performance of the primary interfaces close to 100% is obtained in the floating ice zones, even at low values of SNR. In the interior of the Antarctic ice sheets (including the subglacial lakes regions), detectability is more critical, with at least 85 dB of SNR required for detecting more than 90% of the basal interface and 80% of the IRHs. The condition with the grounded ice in Greenland is the most critical and needs to be explored further, especially to analyze the appropriate frequency dependence of the signal attenuation.

The detectable basal interfaces are also identified as subglacial lakes and bedrock with very high accuracy using an automatic classification algorithm [24] applied to the orbital simulated radargrams. The accuracy is comparable to that of the airborne data, which has been demonstrated for the SNR budget of 85 and 90 dB for illustration purposes. This also shows that existing automatic algorithms for airborne radargrams can be successfully adapted for the extraction of similar information also from the future orbital data. Of course, as in all automatic techniques, there is an intrinsic error rate of the classifier, irrespective of whether the airborne or orbital data are used. The automatic classification depends on the capabilities of the selected training samples to represent the problem in terms of generalization. Hence, varying the training set (e.g., randomly selecting different samples for each experiment) can also result in variations in the accuracy.

As an additional experiment, we have verified the proposed approach by comparing the simulated orbital RS performance obtained from MCoRDS with that obtained from another airborne system [69] having parameters close to the 45-MHz orbital RS. The results of this experiment are presented in Appendix B and show a good agreement between the performance obtained from different airborne radargrams.

Recently, a distributed radar sounder [22] architecture has been proposed, which is based on the deployment of an array of small satellite sensors in a suitable orbital flying configuration. Such an architecture allows the synthesis of very large antenna apertures, thereby significantly improving the along-track resolution, the clutter performance, and the SNR. In particular, the SNR of such a system depends on the antenna gain and transmitted power of individual sensors, and the total number of sensors. Therefore, the performance analysis presented in this article can support and simplify the design of the distributed architecture for an orbital RS. The results presented here can also support a risk assessment of the distributed architecture, such as evaluation of the loss in detection performance due to damage of some of the individual sensors (the resulting loss in SNR budget can be computed, and the corresponding detection performances can be extracted).

For simplicity, the simulation approach proposed here is not integrated with the ionospheric effects and the off-nadir clutter response. However, the losses due to propagation through the ionosphere, roughness of the surface, and volume scattering have been included in the SNR margin. Another performance-limiting factor that has not been considered in this study is the effect of seasonal changes in englacial water storage, which can cause a seasonal increase in the attenuation factor that should be considered in the mission design phase [70], [71]. On the contrary, certain factors degrade the quality of the input airborne radargrams and may lead to underestimation of the orbital RS performance. For example, in the radar equations (1) and (6), we do not consider refraction effects in estimating the subsurface path lengths [52]. These effects are negligible for the orbital RS, while they increase the losses in the case of the airborne systems. Including the refraction effects can improve the orbital RS detection performance, especially over deeper targets, such as the Vostok lake. Moreover, the ARS frames for which the roll angle of the aircraft is significantly high may also be degraded resulting in an underestimation of the orbital RS performance.

These frames could be removed or corrected in future simulations to further improve the accuracy of the performance assessment.

Clutter is an important factor in the selection of the orbital RS frequency, as shown in previous studies [6]. The clutter performance can be integrated into the proposed analysis, by complementing it with the simulation of the cluttergram (using several well-established approaches [30], [32]) over the selected airborne tracks using available digital elevation models (DEMs). The masking of the IRHs by the off-nadir clutter should be considered for evaluating the actual IRH detection performance in terms of SCR. However, in the context of this article, clutter does not significantly influence the SNR budget parameter. Regarding the ionosphere performance, the loss of signal strength and coherence (due to phase errors) may reduce the estimated detection performance in the case of extreme values of TEC. The ionospheric effects can also be easily integrated into the proposed simulation approach using the phase information of the input airborne data and applying the estimated phase distortions as a function of the earth's ionospheric parameters. The integration of ionospheric distortions and clutter simulations into the proposed methodology presents the scope for future research. The results presented here can be further improved by supporting the analysis with laboratory and field measurements of polar ice dielectric properties at UHF and VHF frequencies in order to input more accurate values of the spatially varying Cole–Cole distribution parameter.

The simulated radargrams generated by the proposed method can also be used to test the adaptability of automatic target detection algorithms developed for the airborne data to the orbital case. This has been demonstrated in this article using a subglacial lakes' detection algorithm. In preparation for the scientific interpretation of the data in the advanced phases of development of the mission, the proposed simulation approach can be used to adapt the existing algorithms for applications to the orbital radargrams. As a final remark, it is worth noting that the scientific objectives of an orbiting RS are not restricted to the detection of bedrock, subglacial lakes, and ice shelves. In future activities, we plan to analyze the required conditions for interpreting the basal state, such as frozen or thawed bedrock [46], subglacial water flow channels [4], and the presence of marine ice and cavities at the base of ice shelves [72].

## Appendix A
## SNR Margin Calculations

The proposed simulation approach does not include some of the losses that can be critical for the detection of the ice targets. In order to include their effects in the detectability analysis, we consider an SNR margin of 5 dB, i.e., a subsurface interface is considered to be detected if its SNR is at least 5 dB. In this section, we justify how 5 dB is a conservative SNR margin and is sufficiently higher than the total expected losses.

Let $\mathcal{L}(f_c)$ denote the total loss in power in dB caused by phenomena that are not accurately modeled in the simulation approach and depend on the central frequency $f_c$ of the orbital RS. These include two-way volume scattering

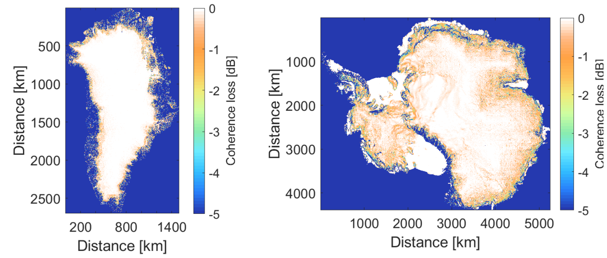


(a) (b)

Fig. 9. Coherence loss estimated over (a) Greenland and (b) Antarctica at a 45-MHz central frequency.

attenuation $\nu(f_c)$, ionospheric effects $\Omega(f_c)$, and coherence loss due to surface roughness $\psi(f_c)$. Out of these, the simulations do not include ionospheric effects while overestimating the volume scattering and coherence losses (the simulation represents these losses around 190–195 MHz, i.e., the central frequency of the ARS, which are expected to be much higher than the losses at 45 MHz, i.e., the orbital RS central frequency). Let us quantitatively examine the overestimation and the missing loss terms one by one.

At $f_c = 45$ MHz, the volume scattering loss is nearly 0, whereas, at $f_c = 195$ MHz, it is about 8 dB ([6, Fig. 16], averaged over a radius of 0–0.5 m of the volume scatterers). The ionospheric peak loss at 45 MHz after ionospheric compensation is reported in Fig. 4 of [17] and ranges between 0.1 and 2 dB during the solar minimum and rises up to 6 dB during extreme events and high errors in TEC estimations during the 11-year solar cycle. For this calculation, we will consider the worst case peak loss of 6 dB in order to be conservative.

The coherence loss due to roughness depends on the surface elevation and slopes of Greenland and Antarctica. We have used 90-m resolution DEM of Greenland [61] and 400-m resolution DEM of Antarctica [73] to first evaluate the slopes at the DEM resolution and estimate the Hurst exponent, which was then used to scale the slopes to a horizontal lag distance of 6.6 m (wavelength at 45 MHz) and 1.5 m (wavelength at 195 MHz) [74]. The coherence loss is related to the slope and is obtained from backscattering models based on Kirchhoff's approximation [75]. Fig. 9 shows the spatial distribution of the estimated coherence losses over Antarctica and Greenland at 45 MHz. Note that the interior of the ice sheets in most of the areas is relatively flat and has a minor contribution to the low coherence loss. The literature values of the slopes obtained with other datasets, including higher resolution DEMs, are consistent or even lower than what we report here [76]–[79]. In any case, we found that the difference between the coherence loss at 45 and 195 MHz is not significant, and it is not changing the SNR margin. We have estimated the average coherence loss at 45 and 195 MHz as 1.56 and 2.22 dB, respectively.

Thus, the total loss at 45 MHz is

$$\begin{aligned}\mathcal{L}(45) &= \nu(45) + \Omega(45) + \psi(45)\\ &= 0 + 6 + 1.56 \approx 8 \text{ dB}.\end{aligned} \tag{15}$$

However, the losses already included in the simulation are

$$\nu(195) + \psi(195) = 8 + 2.22 \approx 10 \text{ dB}. \tag{16}$$

This article has been accepted for inclusion in a future issue of this journal. Content is final as presented, with the exception of pagination.



Therefore, from (15) to (16), we see that there is a net overestimation of 2 dB of losses in the simulated radargrams. To further allow for uncertainties in the ionospheric and volume scattering losses, we have considered an additional SNR margin of 3 dB for assessing the detectability, thus resulting in a total margin of 5 dB over the expected SNR of the targets.

## Appendix B
## Sensitivity Analysis of the Simulation Approach

The simulation technique based on reprocessing available RS data on a geologically similar terrain, which is the basis for the EORS simulations in this article, has been already validated in [21]. In this section, we present an experiment to compare the performance assessment of an orbital RS for a specific case starting from different airborne data to show the reliability and robustness of the proposed approach. The experimental results presented in Section IV have been obtained using as input the data acquired by the airborne MCoRDS-3 instrument, which operates in the UHF band (with central frequency around 195 MHz). However, there exist other airborne instruments, such as the high-capability radar sounder (HiCARS) system [69] operating at a central frequency of 60 MHz with a bandwidth of 15 MHz, and, thus, very close to the parameters of the proposed orbital RS (see Table I). While this is favorable for obtaining more reliable and realistic simulations, the coverage of HiCARS is limited to Antarctica only (this is the reason for which they were not used in this article).

Nevertheless, we have exploited the opportunity presented by the availability of HiCARS data to further validate the proposed methodology. To this purpose, we have selected the following pair of nearly overlapping MCoRDS and HiCARS radargrams: 1) the HiCARS-2 Level 1B time-lagged echo strength profiles data IR2HI1B_2011349_VCD_JKB2g_DVD01a_000 [69], [80] (low and high gain channels were merged before use) and 2) the MCoRDS-3 MVDR processed echoes 20131127_01_032-033 from the 2013_Antarctica_P3 campaign [1] provided by CRESIS (see Table I). These cover a track length of about 80 km in the grounded ice of East Antarctica.

### A. Comparison of Simulated Orbital RS Performance Obtained From Different Airborne Radargrams

Next, starting from the MCoRDS and the HiCARS data, we simulated the radargrams of an orbital RS having the same parameters, as reported in Table I, and using the technique described in Section III-E. Note that the value of $\eta$ is taken as 0.18 since the track is in Antarctica. The two sets of simulated radargrams obtained are referred by the subscript $H{-}E$, i.e., HiCARS to EORS and $M{-}E$, i.e., MCoRDS to EORS. Finally, we compared the primary detection performances in terms of the IRH detection metric and basal interface power. Note that the secondary performance analysis (i.e., detection of subglacial lakes) is implicitly validated because: 1) it depends on the detectability of the basal interface and 2) the underlying classification algorithm has been already validated in [24] using ground-truth data.

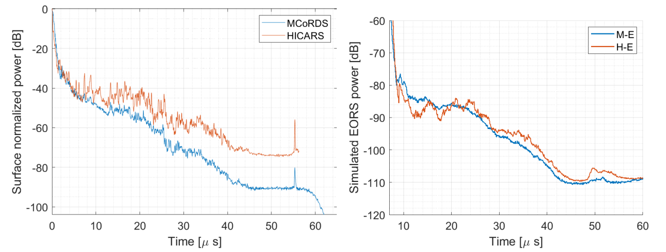


(a) (b)

Fig. 10. Comparison of simulated EORS power: (a) MCoRDS and HiCARS received power profile normalized by the surface echo and (b) simulated received power profile corresponding to $\mathrm{SNR}_b = 80$ dB of the $H{-}E$ and $M{-}E$ cases.

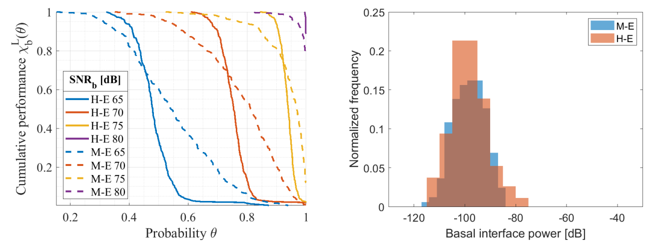


(a) (b)

Fig. 11. Comparison of performance metrics for the EORS simulations obtained from MCoRDS and HiCARS instruments: (a) cumulative distribution of IRH detection performance corresponding to $\mathrm{SNR}_b = \{65, 70, 75, 80\}$ dB and (b) histograms of the basal interface power in the $M{-}E$ and $H{-}E$ simulated radargrams corresponding to $\mathrm{SNR}_b = 85$ dB.

Fig. 10 shows the comparison of the input ARS power profiles (normalized by the surface echo, since the ranges of absolute power in the two datasets are very different) and the simulated EORS received power obtained from MCoRDS and HiCARS. From Fig. 10(b), it is clear that the proposed approach is resulting in a similar power response starting from the different ARS instruments.

Fig. 11(a) shows the cumulative distribution of IRH detection performance, which represents the probability of IRH detection in each frame of the simulated radargrams. Here, we observe a good agreement between the two curves representing $H{-}E$ (solid lines) and $M{-}E$ (dashed lines) for different values of $\mathrm{SNR}_b$, especially for values higher than 70 dB. Above 80 dB, nearly all the layers are detected in both the simulation cases, and hence, these cases have not been shown in the plot. Fig. 11(b) shows the histograms of the basal interface power at $\mathrm{SNR}_b = 85$ dB, showing good agreement between the two cases. Note that we do not report the basal power histograms for all the six values of $\mathrm{SNR}_b$ as they have similar characteristics but the corresponding offset in power.

### B. Analysis of the Impact of the Frequency Dependence Factor on the Simulation Results

We have further analyzed the sensitivity of the simulations to the selected value of the frequency-dependence factor $\eta$ (referred to as the Cole–Cole distribution parameter in [42]). The values of $\eta$ for the analysis are 0.00 (indicating frequency-independent attenuation [49]), 0.08 (reported by [42] and [81] for Greenland), 0.15 (reported by [42] and [59] for Antarctica), 0.18 (reported by [42] and [60]

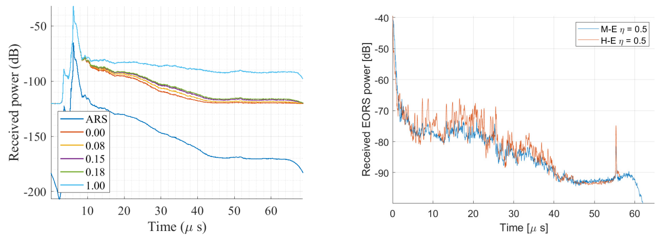


(a) (b)

Fig. 12. Impact of frequency-dependence factor: (a) average received power profile of the simulated radargrams corresponding to different values of $\eta$ and $\text{SNR}_b = 90$ dB. The input airborne data are the MCoRDS-3 radargram 20131127_01_032-033; (b) received EORS power profile after signal magnitude correction applied to HiCARS and MCoRDS data [see Fig. 10(a)] for $\eta = 0.5$ and $\text{SNR}_b = 80$ dB. This value of $\eta$ gives the best agreement between the two cases $H\text{–}E$ and $M\text{–}E$.

for Antarctica), and 1.00 (indicating linearly proportional frequency dependence of the radar attenuation).

Fig. 12(a) shows the average received power profiles of the simulated radargrams obtained from the MCoRDS-3 data 20131127_01_032-033 and corresponding to different values of $\eta$. We observe that, as the value of $\eta$ increases, the received power increases, and the linearly proportional frequency dependence has the highest power among all the cases. For the case of frequency independence or weak dependence, the range of considered $\eta$ values results in a maximum variation of less than 20 dB in the received power. Note that, for the two literature reported values of $\eta = 0.15$ and 0.18 for Antarctica, the difference in the received power is negligible. Furthermore, $\eta$ more strongly impacts the performance of the basal power (and other interfaces close to the base) compared to the near-surface IRHs.

We have also compared the simulated $H\text{–}E$ and $M\text{–}E$ power profiles corresponding to different values of $\eta$. It was found that, for the closest segments along the selected HiCARS and MCoRDS tracks, $\eta = 0.5$ resulted in the best match between the $H\text{–}E$ and $M\text{–}E$ cases, as shown in Fig. 12(b). Since the actual value of $\eta$ can have high spatial variability along the track and in the vertical direction [42], the assumption of a uniform value of $\eta$ for all the simulations may impact the accuracy of the observed detection performance. This needs to be further analyzed by detailed field measurements of the polar ice dielectric properties at different frequencies. In absence of such information, we have used the literature reported values of $\eta$ for the present analysis.

In summary, the aforementioned experiments demonstrate the validity of the proposed performance assessment methodology and further show that the proposed approach is not biased by the choice of the input airborne data (although when possible ARS as similar as possible to the orbital RS should be considered). To show the effectiveness of the methodology, we have presented the comparison for lower level metrics that are more closely related to the simulated radargrams. However, the final performance assessment of an EORS, made on a larger database covering several thousand kilometers of track length and grouped by the geolabels, is expected to be less sensitive to relatively small differences in the simulated radargrams.

## Acknowledgment

The authors would like to thank the three anonymous reviewers whose valuable suggestions greatly helped to improve this article. They would also acknowledge the use of data in part by the Center for Remote Sensing of Ice Sheets (CReSIS) supported from the University of Kansas, NSF, under Grant ANT-0424589; in part by the National Aeronautics and Space Administration (NASA) Operation IceBridge under Grant NNX16AH54G; in part by the use of the High Capability Radar Sounder (HiCARS) lines, funded as a part of NSF's International Polar Year activities to The University of Texas at Austin under Grant ANT-0733025; and in part by the UK's Natural Environment Research Council (NERC) to the University of Edinburgh under Grant NE/D003733/1.

## References

[1] L. Shi *et al.*, "Multichannel coherent radar depth sounder for NASA operation ice bridge," in *Proc. IEEE Int. Geosci. Remote Sensors Symp. (IGARSS)*, Jul. 2010, pp. 1729–1732.

[2] A. Moussessian *et al.*, "A new coherent radar for ice sounding in Greenland," in *Proc. IEEE Int. Geosci. Remote Sens. Symp. Taking Pulse Planet: Role Remote Sens. Manag. Environment. (IGARSS)*, vol. 2, Jul. 2000, pp. 484–486.

[3] D. A. Young, D. M. Schroeder, D. D. Blankenship, S. D. Kempf, and E. Quartini, "The distribution of basal water between Antarctic subglacial lakes from radar sounding," *Phil. Trans. Roy. Soc. A, Math., Phys. Eng. Sci.*, vol. 374, no. 2059, Jan. 2016, Art. no. 20140297. [Online]. Available: https://royalsocietypublishing.org/doi/abs/10.1098/rsta.2014.0297

[4] D. M. Schroeder, D. D. Blankenship, and D. A. Young, "Evidence for a water system transition beneath Thwaites Glacier, West Antarctica," *Proc. Nat. Acad. Sci. USA*, vol. 110, no. 30, pp. 12225–12228, 2013.

[5] R. E. Bell *et al.*, "Deformation, warming and softening of Greenland's ice by refreezing meltwater," *Nature Geosci.*, vol. 7, no. 7, p. 497, 2014.

[6] R. Culberg and D. M. Schroeder, "Firn clutter constraints on the design and performance of orbital radar ice sounders," *IEEE Trans. Geosci. Remote Sens.*, vol. 58, no. 9, pp. 6344–6361, Sep. 2020.

[7] R. Seu *et al.*, "SHARAD: The MRO 2005 shallow radar," *Planet. Space Sci.*, vol. 52, nos. 1–3, pp. 157–166, 2004.

[8] G. Picardi *et al.*, "MARSIS: Mars advanced radar for subsurface and ionosphere sounding," in *Mars Express: The Scientific Payload* (ESA Special Publication), vol. 1240, A. Wilson and A. Chicarro, Eds. Noordwijk, The Netherlands: European Space Agency, Aug. 2004, pp. 51–69.

[9] T. Ono and H. Oya, "Lunar radar sounder (LRS) experiment onboard the SELENE spacecraft," *Earth, Planets Space*, vol. 52, no. 9, pp. 629–637, 2000.

[10] L. Bruzzone *et al.*, "Jupiter ICY moon explorer (JUICE): Advances in the design of the radar for Icy moons (RIME)," in *Proc. IEEE Int. Geosci. Remote Sens. Symp. (IGARSS)*, Jul. 2015, pp. 1257–1260.

[11] D. Blankenship *et al.*, "REASON for Europa," in *Proc. 42nd COSPAR Sci. Assem.*, vol. 42, 2018, pp. B5–3.

[12] L. Bruzzone *et al.*, "STRATUS: Satellite radar sounder for earth subsurface sensing," Final Rep. to STRATUS Project, Italian Space Agency, Italy, 2018.

[13] E. Heggy, P. A. Rosen, R. Beatty, T. Freeman, and Y. Gim, "Exploring desert aquifers and polar ice sheets and their responses to climate evolution: OASIS mission concept," in *Advances in Remote Sensing and Geo Informatics Applications*. Cham, Switzerland: Springer, 2019, pp. 7–10.

[14] A. Freeman, X. Pi, and E. Heggy, "Radar sounding through the Earth's ionosphere at 45 MHz," *IEEE Trans. Geosci. Remote Sens.*, vol. 55, no. 10, pp. 5833–5842, Oct. 2017.

[15] J. Dall, H. F. Corr, N. Walker, B. Rommen, and C.-C. Lin, "Sounding the Antarctic ice sheet from space: A feasibility study based on airborne P-band radar data," in *Proc. IEEE Int. Geosci. Remote Sens. Symp. (IGARSS)*, Jul. 2018, pp. 4142–4145.

[16] L. Bruzzone, G. Alberti, C. Catallo, A. Ferro, W. Kofman, and R. Orosei, "Subsurface radar sounding of the Jovian moon Ganymede," *Proc. IEEE*, vol. 99, no. 5, pp. 837–857, May 2011.

[17] T. Scuccato, L. Carrer, F. Bovolo, and L. Bruzzone, "Compensating Earth ionosphere phase distortion in spaceborne VHF radar sounders for subsurface investigations," *IEEE Geosci. Remote Sens. Lett.*, vol. 15, no. 11, pp. 1672–1676, Nov. 2018.

[18] E. Heggy, G. Scabbia, L. Bruzzone, and R. T. Pappalardo, "Radar probing of Jovian icy moons: Understanding subsurface water and structure detectability in the JUICE and Europa missions," *Icarus*, vol. 285, pp. 237–251, Mar. 2017.

[19] C. Gerekos, A. Tamponi, L. Carrer, D. Castelletti, M. Santoni, and L. Bruzzone, "A coherent multilayer simulator of radargrams acquired by radar sounder instruments," *IEEE Trans. Geosci. Remote Sens.*, vol. 56, no. 12, pp. 7388–7404, Dec. 2018.

[20] E. Sbalchiero, S. Thakur, and L. Bruzzone, "3D radar sounder simulations of geological targets on Ganymede Jovian Moon," in *Image and Signal Processing for Remote Sensing XXV*, vol. 11155, L. Bruzzone and F. Bovolo, Eds. Bellingham, WA, USA: SPIE, 2019, pp. 442–454, doi: 10.1117/12.2533066.

[21] S. Thakur and L. Bruzzone, "An approach to the simulation of radar sounder radargrams based on geological analogs," *IEEE Trans. Geosci. Remote Sens.*, vol. 57, no. 8, pp. 5266–5284, Aug. 2019.

[22] L. Carrer, C. Gerekos, F. Bovolo, and L. Bruzzone, "Distributed radar sounder: A novel concept for subsurface investigations using sensors in formation flight," *IEEE Trans. Geosci. Remote Sens.*, vol. 57, no. 12, pp. 9791–9809, Dec. 2019.

[23] R. E. Bell *et al.*, "Influence of subglacial geology on the onset of a West Antarctic ice stream from aerogeophysical observations," *Nature*, vol. 394, no. 6688, pp. 58–62, 1998.

[24] A.-M. Ilisei, M. Khodadadzadeh, A. Ferro, and L. Bruzzone, "An automatic method for subglacial lake detection in ice sheet radar sounder data," *IEEE Trans. Geosci. Remote Sens.*, vol. 57, no. 6, pp. 3252–3270, Jun. 2019.

[25] E. Donini, S. Thakur, F. Bovolo, and L. Bruzzone, "An automatic approach to map refreezing ice in radar sounder data," *Proc. SPIE*, vol. 11155, Oct. 2019, Art. no. 111551B.

[26] J. Li *et al.*, "High-altitude radar measurements of ice thickness over the Antarctic and Greenland ice sheets as a part of operation ice-bridge," *IEEE Trans. Geosci. Remote Sens.*, vol. 51, no. 2, pp. 742–754, Feb. 2013.

[27] D. Bekaert *et al.*, "Multichannel surface clutter suppression: East Antarctica P-band SAR ice sounding in the presence of grating lobes," *Ann. Glaciol.*, vol. 55, no. 67, pp. 9–21, 2014.

[28] K. C. Jezek *et al.*, "Two-frequency radar experiments for sounding glacier ice and mapping the topography of the glacier bed," *IEEE Trans. Geosci. Remote Sens.*, vol. 49, no. 3, pp. 920–929, Mar. 2011.

[29] J. Dall *et al.*, "ESA's polarimetric airborne radar ice sounder (POLARIS): Design and first results," *IET Radar, Sonar Navigat.*, vol. 4, no. 3, pp. 488–496, 2010.

[30] F. Russo *et al.*, "An incoherent simulator for the SHARAD experiment," in *Proc. IEEE Radar Conf.*, May 2008, pp. 1–4.

[31] P. Choudhary, J. W. Holt, and S. D. Kempf, "Surface clutter and echo location analysis for the interpretation of SHARAD data from Mars," *IEEE Geosci. Remote Sens. Lett.*, vol. 13, no. 9, pp. 1285–1289, Sep. 2016.

[32] Y. A. Ilyushin, R. Orosei, O. Witasse, and B. Sánchez-Cano, "CLUSIM: A synthetic aperture radar clutter simulator for planetary exploration," *Radio Sci.*, vol. 52, no. 9, pp. 1200–1213, 2017.

[33] D. Castelletti *et al.*, "An interferometric approach to cross-track clutter detection in two-channel VHF radar sounders," *IEEE Trans. Geosci. Remote Sens.*, vol. 55, no. 11, pp. 6128–6140, Nov. 2017.

[34] R. Raney, "Radar sounder: Cross-track polarimetric selectivity," in *Proc. 7th Eur. Conf. Synth. Aperture Radar*, Jun. 2008, pp. 1–4.

[35] L. Carrer and L. Bruzzone, "Solving for ambiguities in radar geophysical exploration of planetary bodies by mimicking bats echolocation," *Nature Commun.*, vol. 8, no. 1, p. 2248, 2017.

[36] G. Lewis, E. Osterberg, R. Hawley, B. Whitmore, H. P. Marshall, and J. Box, "Regional Greenland accumulation variability from operation IceBridge airborne accumulation radar," *Cryosphere*, vol. 11, no. 2, pp. 773–788, Mar. 2017.

[37] H. Cane, "Spectra of the non-thermal radio radiation from the galactic polar regions," *Monthly Notice Roy. Astron. Soc.*, vol. 189, no. 3, pp. 465–478, 1979.

[38] F. Hélière, C.-C. Lin, H. Corr, and D. Vaughan, "Radio echo sounding of pine Island Glacier, West Antarctica: Aperture synthesis processing and analysis of feasibility from space," *IEEE Trans. Geosci. Remote Sens.*, vol. 45, no. 8, pp. 2573–2582, Aug. 2007.

[39] A.-M. Ilisei, J. Li, S. Gogineni, and L. Bruzzone, "Estimation of ice sheet attenuation by using radar sounder and ice core data," *Proc. SPIE*, vol. 10004, Oct. 2016, Art. no. 1000416.

[40] O. Brandt, K. Langley, A. Giannopoulos, S. E. Hamran, and J. Kohler, "Radar response of Firn exposed to seasonal percolation, validation using cores and FDTD modeling," *IEEE Trans. Geosci. Remote Sens.*, vol. 47, no. 8, pp. 2773–2786, Aug. 2009.

[41] O. Eisen, F. Wilhelms, U. Nixdorf, and H. Miller, "Revealing the nature of radar reflections in ice: DEP-based FDTD forward modeling," *Geophys. Res. Lett.*, vol. 30, no. 5, pp. 1–4, Mar. 2003.

[42] J. A. MacGregor *et al.*, "Radar attenuation and temperature within the Greenland ice Sheet," *J. Geophys. Res., Earth Surf.*, vol. 120, no. 6, pp. 983–1008, 2015.

[43] K. Matsuoka, J. A. MacGregor, and F. Pattyn, "Predicting radar attenuation within the Antarctic ice sheet," *Earth Planet. Sci. Lett.*, vols. 359–360, pp. 173–183, Dec. 2012.

[44] K. H. Kjær *et al.*, "A large impact Crater beneath Hiawatha glacier in Northwest Greenland," *Sci. Adv.*, vol. 4, no. 11, Nov. 2018, Art. no. eaar8173. [Online]. Available: https://advances.sciencemag.org/content/4/11/eaar8173

[45] J. A. MacGregor *et al.*, "A possible second large subglacial impact Crater in Northwest Greenland," *Geophys. Res. Lett.*, vol. 46, no. 3, pp. 1496–1504, Feb. 2019. [Online]. Available: https://agupubs.onlinelibrary.wiley.com/doi/abs/10.1029/2018GL078126

[46] K. Christianson *et al.*, "Basal conditions at the grounding zone of Whillans ice stream, West Antarctica, from ice-penetrating radar," *J. Geophys. Res.: Earth Surf.*, vol. 121, no. 11, pp. 1954–1983, Nov. 2016.

[47] E. Pettinelli *et al.*, "Dielectric properties of Jovian satellite ice analogs for subsurface radar exploration: A review," *Rev. Geophys.*, vol. 53, no. 3, pp. 593–641, 2015. [Online]. Available: https://agupubs.onlinelibrary.wiley.com/doi/abs/10.1002/2014RG000463

[48] J. G. Paren and G. D. Q. Robin, "Internal reflections in polar ice sheets," *J. Glaciol.*, vol. 14, no. 71, pp. 251–259, 1975.

[49] S. Fujita, T. Matsuoka, T. Ishida, K. Matsuoka, and S. Mae, "A summary of the complex dielectric permittivity of ice in the megahertz range and its applications for radar sounding of polar ice sheets," in *Physics of Ice Core Records*. Sapporo, Japan: Hokkaido Univ. Press, 2000, pp. 185–212.

[50] N. Holschuh, K. Christianson, and S. Anandakrishnan, "Power loss in dipping internal reflectors, imaged using ice-penetrating radar," *Ann. Glaciol.*, vol. 55, no. 67, pp. 49–56, 2014.

[51] M. S. Haynes, E. Chapin, and D. M. Schroeder, "Geometric power fall-off in radar sounding," *IEEE Trans. Geosci. Remote Sens.*, vol. 56, no. 11, pp. 6571–6585, Nov. 2018.

[52] M. S. Haynes, "Surface and subsurface radar equations for radar sounders," *Ann. Glaciol.*, vol. 61, no. 81, pp. 135–142, Apr. 2020.

[53] L. Carrer and L. Bruzzone, "Automatic enhancement and detection of layering in radar sounder data based on a local scale hidden Markov model and the Viterbi algorithm," *IEEE Trans. Geosci. Remote Sens.*, vol. 55, no. 2, pp. 962–977, Feb. 2017.

[54] S. Xiong, J.-P. Muller, and R. Carretero, "A new method for automatically tracing englacial layers from MCoRDS data in NW Greenland," *Remote Sens.*, vol. 10, no. 2, p. 43, Dec. 2017.

[55] A. Ferro and L. Bruzzone, "Automatic extraction and analysis of ice layering in radar sounder data," *IEEE Trans. Geosci. Remote Sens.*, vol. 51, no. 3, pp. 1622–1634, Mar. 2013.

[56] A. Ferro and L. Bruzzone, "Analysis of radar sounder signals for the automatic detection and characterization of subsurface features," *IEEE Trans. Geosci. Remote Sens.*, vol. 50, no. 11, pp. 4333–4348, Nov. 2012.

[57] A. M. Ilisei and L. Bruzzone, "A system for the automatic classification of ice sheet subsurface targets in radar sounder data," *IEEE Trans. Geosci. Remote Sens.*, vol. 53, no. 6, pp. 3260–3277, Jun. 2015.

[58] P. S. Tan, J. Paden, J. Li, J.-B. Yan, and P. Gogineni, "Robust adaptive MVDR beamforming for processing radar depth sounder data," in *Proc. IEEE Int. Symp. Phased Array Syst. Technol.*, Oct. 2013, pp. 622–629.

[59] J. D. Paden, C. T. Allen, S. Gogineni, K. C. Jezek, D. Dahl-Jensen, and L. B. Larsen, "Wideband measurements of ice sheet attenuation and basal scattering," *IEEE Geosci. Remote Sens. Lett.*, vol. 2, no. 2, pp. 164–168, Apr. 2005.

[60] T. Barrella, S. Barwick, and D. Saltzberg, "Ross ice shelf (Antarctica) *in situ* radio-frequency attenuation," *J. Glaciology*, vol. 57, no. 201, pp. 61–66, 2011.

[61] I. M. Howat, A. Negrete, and B. E. Smith, "The Greenland ice mapping project (GIMP) land classification and surface elevation data sets," *Cryosphere*, vol. 8, no. 4, pp. 1509–1518, Aug. 2014.

[62] K. Matsuoka, A. Skoglund, and G. Roth, "Quantarctica," Norwegian Polar Inst., Tromsø, Norway, Tech. Rep. 10, 2018. [Online]. Available: https://doi.org/10.21334/npolar.2018.8516e961

[63] I. Howat, *MEaSUREs Antarctic Boundaries for IPY 2007-2009 from Satellite Radar, Version 2*. Boulder, Colorado USA. NASA National Snow and Ice Data Center Distributed Active Archive Center. Accessed: Sep. 12, 2019. [Online]. Available: https://nsidc.org/data/NSIDC-0709/versions/2

[64] E. Rignot, S. Jacobs, J. Mouginot, and B. Scheuchl, "Ice-shelf melting around Antarctica," *Science*, vol. 341, no. 6143, pp. 266–270, Jul. 2013. [Online]. Available: https://science.sciencemag.org/content/341/6143/266

[65] E. J. MacKie, D. M. Schroeder, J. Caers, M. R. Siegfried, and C. Scheidt, "Antarctic topographic realizations and geostatistical modeling used to map subglacial lakes," *J. Geophys. Res.: Earth Surf.*, vol. 125, no. 3, Mar. 2020. [Online]. Available: https://agupubs.onlinelibrary.wiley.com/doi/abs/10.1029/2019JF005420

[66] A. Wright and M. J. Siegert, "A fourth inventory of Antarctic subglacial lakes," *Antarctic Sci.*, vol. 24, no. 6, pp. 659–664, 2012.

[67] D. Blankenship, S. Carter, J. Holt, D. Morse, M. Peters, and D. Young, "Antarctic subglacial lake classification inventory," Nat. Snow Ice Data Center, Boulder, CO, USA, Tech. Rep. Final, 2009.

[68] M. Studinger *et al.*, "Ice cover, landscape setting, and geological framework of lake Vostok, East Antarctica," *Earth Planet. Sci. Lett.*, vol. 205, nos. 3–4, pp. 195–210, Jan. 2003.

[69] D. D. Blankenship *et al.* (2017). *IceBridge HiCARS 2 L1B Time-Tagged Echo Strength Profiles, Version 1. Subset*. Accessed: Feb. 12, 2021. [Online]. Available: https://IR2HI1B_2011349_VCD_JKB2g_DVD01a_000

[70] A. K. Kendrick *et al.*, "Surface meltwater impounded by seasonal englacial storage in West Greenland," *Geophys. Res. Lett.*, vol. 45, no. 19, pp. 10–474, Oct. 2018.

[71] W. Chu, D. M. Schroeder, and M. R. Siegfried, "Retrieval of englacial Firn aquifer thickness from ice-penetrating radar sounding in Southeastern Greenland," *Geophys. Res. Lett.*, vol. 45, no. 21, pp. 11770–11778, 2018. [Online]. Available: https://agupubs.onlinelibrary.wiley.com/doi/abs/10.1029/2018GL079751

[72] H. A. Fricker, S. Popov, I. Allison, and N. Young, "Distribution of marine ice beneath the Amery ice shelf," *Geophys. Res. Lett.*, vol. 28, no. 11, pp. 2241–2244, Jun. 2001.

[73] H. Liu, K. C. Jezek, B. Li, and Z. Zhao, "Radarsat Antarctic mapping project digital elevation model, version 2," NASA Nat. Snow Ice Data Center Distrib. Act. Arch. Center, Boulder, CO, USA, Tech. Rep. Final, 2015.

[74] M. K. Shepard, B. A. Campbell, M. H. Bulmer, T. G. Farr, L. R. Gaddis, and J. J. Plaut, "The roughness of natural terrain: A planetary and remote sensing perspective," *J. Geophys. Res., Planets*, vol. 106, no. E12, pp. 32777–32795, Dec. 2001.

[75] J. A. Ogilvy and H. M. Merklinger, "Theory of wave scattering from random rough surfaces," *Acoust. Soc. Amer. J.*, vol. 90, no. 6, p. 3382, Dec. 1991, doi: 10.1121/1.401410.

[76] C. Porter *et al.* (2018). *ArcticDEM, Polar Geospatial Center, Harvard Dataverse, V1*. Accessed: Feb. 2, 2021. [Online]. Available: https://dataverse.harvard.edu/dataset.xhtml?persistentId=doi:10.7910/DVN/OHHUKH

[77] I. M. Howat, C. Porter, B. E. Smith, M.-J. Noh, and P. Morin, "The reference elevation model of Antarctica," *Cryosphere*, vol. 13, no. 2, pp. 665–674, Feb. 2019.

[78] C. J. van der Veen, Y. Ahn, B. M. Csatho, E. Mosley-Thompson, and W. B. Krabill, "Surface roughness over the northern half of the Greenland ice sheet from airborne laser altimetry," *J. Geophys. Res.*, vol. 114, no. F1, 2009.

[79] D. Yi, H. J. Zwally, and X. Sun, "ICESat measurement of Greenland ice sheet surface slope and roughness," *Ann. Glaciol.*, vol. 42, no. 1, pp. 83–89, Aug. 2005.

[80] M. G. P. Cavitte *et al.*, "Deep radiostratigraphy of the East Antarctic plateau: Connecting the dome c and vostok ice core sites," *J. Glaciol.*, vol. 62, no. 232, pp. 323–334, Apr. 2016.

[81] J. C. Hanson *et al.*, "Radar absorption, basal reflection, thickness and polarization measurements from the Ross ice shelf, Antarctica," *J. Glaciol.*, vol. 61, no. 227, pp. 438–446, 2015.


**Sanchari Thakur** (Member, IEEE) received the B.E. degree in civil engineering from Birla Institute of Technology and Science at Pilani, Pilani, India, in 2014, the M.Tech. degree in geoinformatics and natural resources engineering from IIT Bombay, Mumbai, India, in 2016, and the Ph.D. degree in information and communication technology from the Universitá degli Studi di Trento, Trento, Italy, in 2020.

She is currently a Post-Doctoral Researcher with the Remote Sensing Laboratory, Universitá degli Studi di Trento, where she is also working on the design and performance analysis of the subsurface radar sounder onboard ESA's EnVision mission to Venus. Her Ph.D. thesis, titled "Advanced methods for simulation and performance analysis of planetary radar sounder data" was focused on developing and applying radar sounder simulators for the radar for icy moon exploration onboard ESA's JUICE mission, and future terrestrial radar sounder missions. As part of her master's thesis, she worked on a project cosponsored by the United Nation's International Atomic Energy Agency (IAEA) to study spatial statistical properties of global uranium deposits and contributed two chapters to the Quantitative and Spatial Evaluations of Undiscovered Uranium Resources (IAEA-TECDOC-1861). Her research interests include radar sounders, performance simulation, geological interpretation, and analysis of multispectral and radar remote sensing data for the earth and planetary science-based applications.

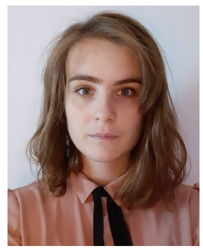

**Elena Donini** (Member, IEEE) received the B.Sc. degree in electronics and telecommunication engineering, the M.Sc. degree *(summa cum laude)* in telecommunication engineering, and the Ph.D. degree *(cum laude)* in information and communication technologies from the University of Trento, Trento, Italy, in 2015, 2017, and 2021, respectively.

She is currently a Post-Doctoral Researcher and a member of the Remote Sensing Laboratory, Department of Information and Communication Technologies, University of Trento, and the Remote Sensing for Digital Earth Unit, Fondazione Bruno Kessler, Trento. Her research interests include the automatic analysis of terrestrial and planetary radar sounder data with machine learning and deep learning techniques.

Dr. Donini is also a member of the scientific team working on the radar for the icy moon exploration (RIME) instrument that will be onboard the upcoming ESA mission JUICE (JUpiter ICy moons explorer) to the Jupiter system. She was a recipient of the prize for the 2017 Best Italian Master Thesis in remote sensing awarded by the Italy Chapter of the IEEE Geoscience and Remote Sensing Society.

**Francesca Bovolo** (Senior Member, IEEE) received the Laurea (B.S.) degree, the Laurea Specialistica (M.S.) degree *(summa cum laude)* in telecommunication engineering, and the Ph.D. degree in communication and information technologies from the University of Trento, Trento, Italy, in 2001, 2003, and 2006, respectively.

She was a Research Fellow with the University of Trento until 2013. She is currently the Founder and the Head of the Remote Sensing for Digital Earth Unit, Fondazione Bruno Kessler, Trento, and a member of the Remote Sensing Laboratory, Trento. She is one of the coinvestigators of the Radar for Icy Moon Exploration instrument of the European Space Agency Jupiter Icy Moons Explorer and a member of the science study team of the EnVision mission to Venus. Her research interests include remote-sensing image processing; multitemporal remote sensing image analysis; change detection in multispectral, hyperspectral, and synthetic aperture radar images; and very high-resolution images, time series analysis, content-based time series retrieval, domain adaptation, and light detection and ranging (LiDAR) and radar sounders. She conducts research on these topics within the context of several national and international projects.

Dr. Bovolo is also a member of the program and scientific committee of several international conferences and workshops. She was a recipient of the First Prize in the Student Prize Paper Competition of the 2006 IEEE International Geoscience and Remote Sensing Symposium (Denver, 2006). She was the Technical Chair of the Sixth International Workshop on the Analysis of Multitemporal Remote-Sensing Images (MultiTemp 2011, and 2019). She has been the Co-Chair of the SPIE International Conference on Signal and Image Processing for Remote Sensing since 2014. She is also the Publication Chair of the International Geoscience and Remote Sensing Symposium in 2015. She has been an Associate Editor of the IEEE JOURNAL OF SELECTED TOPICS IN APPLIED EARTH OBSERVATIONS AND REMOTE SENSING since 2011 and the Guest Editor of the Special Issue on Analysis of Multitemporal Remote Sensing Data of the IEEE TRANSACTIONS ON GEOSCIENCE AND REMOTE SENSING. She is also a referee of several international journals.

**Lorenzo Bruzzone** (Fellow, IEEE) received the Laurea (M.S.) degree *(summa cum laude)* in electronic engineering and the Ph.D. degree in telecommunications from the University of Genoa, Genoa, Italy, in 1993 and 1998, respectively.

He is currently a Full Professor of telecommunications with the University of Trento, Trento, Italy, where he teaches remote sensing, radar, and digital communications. He is also the Founder and the Director of the Remote Sensing Laboratory (https://rslab.disi.unitn.it/), Department of Information Engineering and Computer Science, University of Trento. He is the author (or coauthor) of 294 scientific publications in refereed international journals (221 in IEEE journals), more than 340 papers in conference proceedings, and 22 book chapters. His articles are highly cited, as proven from the total number of citations (more than 39 000) and the value of the H-index (91) (source: Google Scholar). He was invited as a keynote speaker in more than 40 international conferences and workshops. His current research interests include remote sensing, radar and SAR, signal processing, machine learning, and pattern recognition. He promotes and supervises research on these topics within the frameworks of many national and international projects. He is also the principal investigator of many research projects. Among the others, he is also the Principal Investigator of the radar for icy moon exploration (RIME) instrument in the framework of the JUpiter ICy moons explorer (JUICE) mission of the European Space Agency (ESA) and the Science Lead for the High Resolution Land Cover Project in the framework of the Climate Change Initiative of ESA.

Dr. BruzzoneDr. Bruzzone has been a member of the Administrative Committee of the IEEE Geoscience and Remote Sensing Society (GRSS) since 2009, where, since 2019, he has also been the Vice President of professional activities. He is also a member of the Permanent Steering Committee of this series of workshops. He is also the Co-Founder of the IEEE International Workshop on the Analysis of Multi-Temporal Remote-Sensing Images (MultiTemp) series. He ranked first place in the Student Prize Paper Competition of the 1998 IEEE International Geoscience and Remote Sensing Symposium (IGARSS), Seattle, WA, USA, in July 1998. Since that, he was a recipient of many international and national honors and awards, including the recent IEEE GRSS 2015 Outstanding Service Award, the 2017 and 2018 IEEE IGARSS Symposium Prize Paper Awards, and the 2019 WHISPER Outstanding Paper Award. Since 2003, he has been the Chair of the SPIE Conference on Image and Signal Processing for Remote Sensing. He had been the Founder of *IEEE Geoscience and Remote Sensing Magazine* for which he had been the Editor-in-Chief from 2013 to 2017. He was the guest co-editor of many special issues of international journals. He is also an editor/co-editor of 18 books/conference proceedings and one scientific book. He is also an Associate Editor of the IEEE TRANSACTIONS ON GEOSCIENCE AND REMOTE SENSING. He had been the Distinguished Speaker of the IEEE Geoscience and Remote Sensing Society from 2012 to 2016.